

# Surface Noble Metal Concentration on Ceria as a Key Descriptor for Efficient Catalytic CO Oxidation

Florian Maurer,<sup>#</sup> Arik Beck,<sup>#</sup> Jelena Jelic, Wu Wang, Stefan Mangold, Matthias Stehle, Di Wang, Paolo Dolcet, Andreas M. Gänzler, Christian Kübel, Felix Studt, Maria Casapu, and Jan-Dierk Grunwaldt<sup>\*</sup>



Cite This: *ACS Catal.* 2022, 12, 2473–2486



Read Online

ACCESS |



Metrics & More



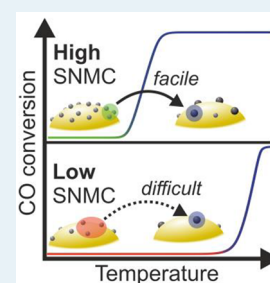
Article Recommendations



Supporting Information

**ABSTRACT:** During the CO oxidation over metallic Pt clusters and Pt nanoparticles in Pt/CeO<sub>2</sub> catalysts, we found that the Pt surface concentration is a key descriptor for the reaction rate. By increasing the surface noble metal concentration (SNMC) of a Pt/CeO<sub>2</sub> catalyst by a factor of ~4, while keeping the weight hourly space velocity constant, the ignition temperature of CO oxidation was decreased by ~200 °C in the as-prepared state. Moreover, the stability was enhanced at higher SNMC. Complementary characterization and theoretical calculations unraveled that the origin of this improved reaction rate at higher Pt surface concentrations can be traced back to the formation of larger oxidized Pt-clusters and the SNMC-dependent aggregation rate of highly dispersed Pt species. The Pt diffusion barriers for cluster formation were found to decrease with increasing SNMC, promoting more facile agglomeration of active, metallic Pt particles. In contrast, when Pt particle formation was forced with a reductive pretreatment, the influence of the SNMC was temporarily diminished, and all catalysts showed a similar CO oxidation activity. The work shows the general relevance of the proximity influence in the formation and stabilization of active centers in heterogeneous catalysis.

**KEYWORDS:** *In situ* characterization, nanoparticle formation, Raman spectroscopy, X-ray absorption spectroscopy, surface diffusion, proximity effect, surface noble metal concentration



## 1. INTRODUCTION

Platinum group metals supported as nanoparticles (NPs) on metal oxide carriers are employed in environmental and hydrogenation catalysis, electrocatalysis, or energy-related processes.<sup>1–4</sup> High-surface-area carriers are typically used to stabilize the NPs, which ensures a high ratio of surface-to-bulk atoms for the active species. During the last decades, the role of the oxide support was reassessed from a broader perspective: the carrier also plays a key role for the catalytic activity, selectivity, and stability of catalysts.<sup>5–8</sup> For instance, redox active supports like CeO<sub>2</sub><sup>9–12</sup> have been intensively investigated, and different descriptors are proposed to influence catalytic performance: morphology/exposed facets,<sup>13–17</sup> porosity,<sup>18–20</sup> reducibility of surface and bulk species,<sup>8,21–23</sup> or noble metal particle size.<sup>24–26</sup> Furthermore, the strong noble metal–support interaction<sup>27–29</sup> is reported to tremendously affect the activity profile. Recent in-depth *in situ* and *operando* characterization and theoretical modeling revealed the inherent dynamics of such catalytic systems under reaction conditions, which further increases their complexity.<sup>8,26,30–33</sup> This includes the evolution of the platinum species themselves but also noble-metal induced reconstruction of the support.<sup>22,24,28,34–37</sup> The dynamics make the catalyst a strongly changing system that responds to the surrounding conditions.<sup>7,33,38–40</sup> Central to the Pt/CeO<sub>2</sub> catalyst is the formation of isolated Pt species on the CeO<sub>2</sub> surface when the catalyst is exposed to oxygen at high temperatures. This

phenomenon leads to the disintegration of the more active Pt nanoparticles.<sup>8,38,40–43</sup> The reverse process occurs under reducing conditions, when monatomic Pt species reaggregate to form Pt nanoparticles.<sup>22,24,44</sup> Both processes occur in emission control catalysis. Whereas pollutants like carbon monoxide and hydrocarbons act as reducing agents (especially at  $\lambda < 1$ ), molecular oxygen is a strong oxidant particularly under lean conditions ( $\lambda > 1$ ).

Another parameter, which to date has rarely been considered,<sup>43,45,46</sup> is the noble metal loading per specific surface area which is related to the proximity of noble metal atoms/clusters/particles on the support surface area unit. To estimate this potential influence, we gathered reported CO oxidation activities for Pt/CeO<sub>2</sub> catalysts from several studies.<sup>41,42,45,47–61</sup> As shown in Figure 1, an impact of the noble metal loading per specific surface area on the catalyst activity (normalized to the total amount of Pt) can be speculated: higher reaction rates per Pt seem to be obtained for catalysts with high Pt loading-to-

Received: October 4, 2021

Revised: December 15, 2021

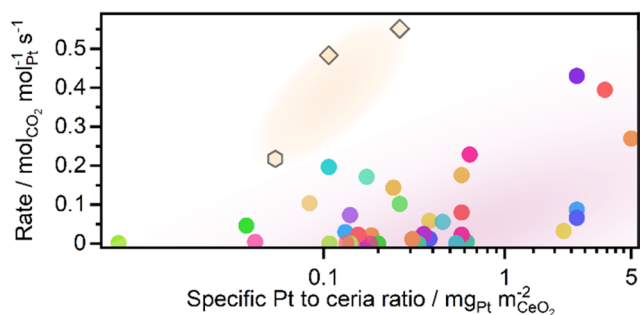


**Figure 1.** CO oxidation rates of various Pt/CeO<sub>2</sub> catalysts investigated in previous studies (different colors)<sup>41,42,45,47–61</sup> in relation to their Pt concentration per support surface area. The three Pt/CeO<sub>2</sub> catalysts indicated by hollowed icons were prerduced prior to catalytic tests. Red and yellow shadowing was used as guide to the eye to indicate the different rate-regions for prerduced and as-prepared/oxidized catalysts.

CeO<sub>2</sub> surface area ratios. Outliers with very high rates are found for prerduced catalysts (polygonal symbols in Figure 1). Yet, also at similar surface loadings for catalysts in the oxidized state, strong variations in the rates exist between the various studies. This may arise due to the preparation procedure or the very different reaction conditions applied such as heating rate or gas composition. It is therefore important to further elaborate whether there is a possible correlation between the surface noble metal concentration (SNMC) and catalyst activity using a systematic approach.

A series of Pt/CeO<sub>2</sub> catalysts containing different noble metal loadings (1.0–4.5 wt %) on CeO<sub>2</sub><sup>38</sup> was prepared and used to study the influence of the SNMC on the CO oxidation activity. For a more facile characterization of the Pt NPs and to minimize additional effects, CeO<sub>2</sub> with a defined morphology (i.e., rod-shaped CeO<sub>2</sub>) was used as support. The SNMC was correlated with the CO oxidation activity, in particular, the ignition temperature of the reaction. To unravel the origin of the identified dependence, the structural and electronic properties of the Pt species were tracked during interaction with the gas phase using *in situ* X-ray absorption, Raman, and infrared spectroscopy. Complementary to these SNMC-structure-activity relations, we applied density functional theory calculations to investigate the role of diffusion barriers of highly dispersed Pt species on CeO<sub>2</sub> and their influence on the catalytic performance. By this systematic approach, we found that the formation of active Pt-clusters from highly dispersed Pt species under reaction conditions is strongly dependent on the proximity of these species to each other. This is essential for catalytic activity, and thus, the SMNC is a key descriptor for designing supported noble metal catalysts.

## 2. EXPERIMENTAL SECTION

**2.1. Catalyst Synthesis.** The synthesis of rod-shaped CeO<sub>2</sub> was carried out according to the procedure developed by Mai et al.<sup>62</sup> using autoclaves (DAB-3, Berghof,  $V = 250$  mL,  $T_{\max} = 250$  °C,  $p_{\max} = 200$  bar) with a Teflon inlay. Initially, 22.03 g of NaOH (VWR Chemicals) was dissolved in 90 mL of deionized H<sub>2</sub>O (6.1 M). Then 1.96 g of Ce(NO<sub>3</sub>)<sub>3</sub>·6 H<sub>2</sub>O (99%, Sigma-Aldrich) was added to the solution and stirred for 10 min. The autoclave was closed and placed in an oven at 100 °C for 21 h. Subsequently, the solid was separated by filtration and washed with 400 mL of deionized water and dried for 12 h at 70 °C. Pt was loaded onto the CeO<sub>2</sub> by incipient wetness impregnation.

(NH<sub>3</sub>)<sub>4</sub>Pt(NO<sub>3</sub>)<sub>2</sub> (99%, Alfa Aesar) was dissolved in purified water (purified water, ROTIPURAN). The Pt solution was added dropwise to the CeO<sub>2</sub> powder in a mortar under constant grinding. To determine the solution volume per impregnation step, the pore volume of the support was determined via N<sub>2</sub> physisorption to be 0.37 cm<sup>3</sup> g<sup>-1</sup>. After each impregnation step, the powder was dried at 60 °C for 20 min. Then, further Pt solution was added, until the desired loading of Pt was obtained. Subsequently, the powder was calcined at 600 °C for 5 h (10 °C min<sup>-1</sup> heating ramp). The Pt loading was confirmed via inductively coupled plasma optical emission spectroscopy (ICP-OES) using a 720/725 emission spectrometer (Agilent).

Samples referred to as “reduced” were loaded into a quartz reactor tube of a tubular furnace and heated in a flow of 2% H<sub>2</sub> in N<sub>2</sub> to 400 °C (10 °C min<sup>-1</sup>) and held there for 30 min at this temperature. Subsequently, the samples were cooled to room temperature in the reducing gas mixture.

**2.2. Light-Off Experiments.** The catalyst bed was prepared in quartz tubes (outer diameter: 10 mm; inner diameter: 8 mm) by diluting the catalyst sieved fraction (grain size of 125–250 μm) with SiO<sub>2</sub> (sieve fraction: 125–250 μm) to 1 g in total. The amount of catalyst was adjusted to the amount of Pt resulting in a constant weight hourly space velocity (WHSV) of 60 000 L g<sub>Pt</sub><sup>-1</sup> h<sup>-1</sup> for all samples. The catalyst bed was fixed in the quartz tube with two quartz wool plugs. Two thermocouples inside the reactor tube monitored the temperature upstream and downstream of the catalyst bed (approximately 1 cm distance to the catalyst bed). The reaction gas mixture was dosed using mass flow controllers (MFC, Bronkhorst) and contained 1000 ppm of CO, 8% O<sub>2</sub>, balanced in N<sub>2</sub>. At the reactor outlet, the gas composition was analyzed with a Fourier-transform infrared spectrometer (FTIR, MKS Instruments). The CO oxidation light-off activities were monitored in the range of 50–500 °C with a heating rate of 10 °C min<sup>-1</sup>. After each light-off, the catalyst was kept at 500 °C for 1 h before it was cooled. After three consecutive light-offs, the catalyst was cooled to 70 °C. As a next step, the gas mixture was switched to a reductive mixture (2% H<sub>2</sub>/N<sub>2</sub>, WHSV: 60 000 L g<sub>Pt</sub><sup>-1</sup> h<sup>-1</sup>) and the catalyst was heated to 400 °C (10 °C min<sup>-1</sup>) and was kept there for 30 min before it was cooled in the reductive atmosphere. After the reductive treatment, once again three consecutive light-off activity profiles (conditions as described above) were recorded. The reaction rate and activation energy ( $E_A$ ) for the first light-off in each series were estimated using an Arrhenius approach, retrieving the rates from CO conversions between 5 and 10%.

**2.3. Transmission Electron Microscopy.** The catalyst powders were directly dispersed on copper grids covered with a holey carbon film. The microstructures of the catalysts were characterized by high angle annular dark-field scanning transmission electron microscopy (HAADF-STEM) in a FEI Titan 80-300 microscopy operated at 300 kV. The Pt particle size statistics of the specimens (counting >100 particles) were determined on HAADF-STEM images by using the Fiji<sup>63</sup> software.

**2.4. Raman Spectroscopy.** Raman spectroscopy was performed with an inVia Reflex spectrometer system (Renishaw) equipped with a research-grade Leica DM2500 microscope and a helium neon laser operating at 633 nm (25 mW at the source). The data was collected in a spectral range from around 100 to 1300 cm<sup>-1</sup> with a resolution of ca. 1 cm<sup>-1</sup> by means of an 1800 lines mm<sup>-1</sup> grating. For the *ex situ* measurements, a 50× Leica objective was used. Furthermore, the laser was defocused to form a line, and at 50% laser intensity,

an area of about  $260 \times 190 \mu\text{m}^2$  was scanned with  $1.3 \mu\text{m}$  raster step size ( $200 \times 150$  collections). Thus, 30 000 spectra were recorded with 60 s acquisition time per spectrum. The Raman spectroscopy data was processed using the software WiRE 4.4 (Renishaw). Every spectrum was initially treated for cosmic ray removal and subsequent noise filtering. For spatially resolved analysis of the Raman data, the spectra were additionally truncated to a range of 250 to  $900 \text{ cm}^{-1}$  and analyzed individually. For integral analysis, the individual spectra were averaged yielding one spectrum per sample.

**2.5.  $\text{N}_2$  Physisorption.** The surface area and pore volume were determined by  $\text{N}_2$  physisorption at  $-196 \text{ }^\circ\text{C}$  according to the Brunauer–Emmett–Teller (BET)<sup>64</sup> method using a multipoint measurement on a BELSORP-mini instrument (MicrotracBEL, Osaka, Japan). Prior to the analysis, all of the samples were degassed at  $300 \text{ }^\circ\text{C}$  for 2 h under reduced pressure. Adsorption isotherms were evaluated in the pressure range of  $p/p_0 = 0.05$  to 0.3.

**2.6.  $\text{H}_2$ -Temperature-Programmed Reduction Using a TCD.** Powder catalyst samples (150 mg of each) were loaded in a quartz tube reactor. Prior to the temperature-programmed reduction (TPR) experiment, the samples were heated in 20%  $\text{O}_2/\text{N}_2$  to  $500 \text{ }^\circ\text{C}$  ( $10 \text{ }^\circ\text{C min}^{-1}$ ). At  $500 \text{ }^\circ\text{C}$ , the samples were held for 1 h. After they were cooled  $50 \text{ }^\circ\text{C}$ , the samples were exposed to 10%  $\text{H}_2/\text{N}_2$ . The outlet gas was monitored with a thermal conductivity detector (TCD) with a  $\text{H}_2\text{O}$  trap in front of the detector. As soon as the detector signal was stable, the samples were heated to  $350 \text{ }^\circ\text{C}$  ( $5 \text{ }^\circ\text{C min}^{-1}$ ). The amount of consumed  $\text{H}_2$  was derived using a calibration curve obtained from the reduction of  $\text{Ag}_2\text{O}$ .

**2.7. X-ray Absorption Spectroscopy.** *Ex situ* extended X-ray absorption fine structure (EXAFS) spectroscopy measurements were performed at the CAT-ACT-beamline<sup>65</sup> (Accelerator Test Facility and Synchrotron Radiation source at KIT, Karlsruhe, Germany) in fluorescence mode using a silicon drift detector (SDD, Vortex-90EX X-ray detector). The energy of the incident X-ray beam was tuned by a double crystal monochromator (DCM) with Si(111) crystals. The size of the X-ray beam on the sample was set to approximately  $1 \times 1 \text{ mm}^2$  using slits. The samples were diluted with cellulose and pressed to pellets. For each sample, 4 spectra were recorded and merged. For the EXAFS fitting, the parameters were restricted (further details given in the electronic Supporting Information (SI), Supporting Table 1): The coordination number was limited to a range between 0 and the degeneracy of the respective path (Supporting Table 2), while the Debye–Waller factor was restricted to positive values between 0.001 and 0.01. The number of fitting variables was reduced by sharing the same mean square deviation  $\sigma^2$  and adjustment of the half path length  $\Delta R$  for paths with a similar effective distance  $R_{\text{eff}}$ . All three samples were fitted in parallel and shared the same energy shift as well as mean square displacement  $\sigma^2$  for paths with a similar effective distance  $R_{\text{eff}}$ . The experimental data in a  $k$ -range of  $2.5\text{--}11.2 \text{ \AA}^{-1}$  were fitted in  $R$ -space ( $1.1\text{--}3.4 \text{ \AA}$ ) with a  $k$ -weighting of 1, 2, and 3. For all samples, the highest fit quality (cf. SI, Figure S2, Supporting Tables 3 and 4) was achieved for the structure model, which assumed a mixture of  $\text{PtO}_x$ -clusters and atomically dispersed Pt-species in  $\text{CeO}_2$ -hollow sites (Figure S1).

*In situ* X-ray absorption near edge structure (XANES) spectra at the Pt  $L_3$ -edge were recorded at the XAS-beamline (Accelerator Test Facility and Synchrotron Radiation source at KIT, Karlsruhe, Germany) in fluorescence mode (SDD, Vortex-90EX X-ray detector). The height of the X-ray beam,

which was pitched in energy by an Si(111) DCM, was 1.0 mm on the sample, and its width was 5.0 mm. A capillary micro reactor heated by a hot air blower (Leister) was used as an *in situ* cell.<sup>66</sup> A heating rate of  $3 \text{ }^\circ\text{C min}^{-1}$  was applied while collecting one XAS spectrum every  $\sim 20 \text{ }^\circ\text{C}$ . Gases (overall flow of  $70 \text{ mL min}^{-1}$ ) were dosed by mass flow controllers (Bronkhorst). The gas concentration at the reactor outlet was monitored online by a mass spectrometer (OmniStar GSD 320, Pfeiffer Vacuum). The temperature-programmed reduction was performed in 2%  $\text{H}_2/\text{He}$  with a WHSV of  $60\,000 \text{ L g}_{\text{Pt}}^{-1} \text{ h}^{-1}$ . For the *in situ* reduction tests, the capillary reactor (1.5 mm outer diameter, 1.48 mm inner diameter) was loaded with 7–8 mg of the granulated ( $100\text{--}200 \mu\text{m}$ ) Pt/CeO<sub>2</sub> catalyst sample. This ensures that internal and external mass transport requirements are fulfilled. The PtO<sub>2</sub> reference was measured as pellet, the Pt reference as foil.

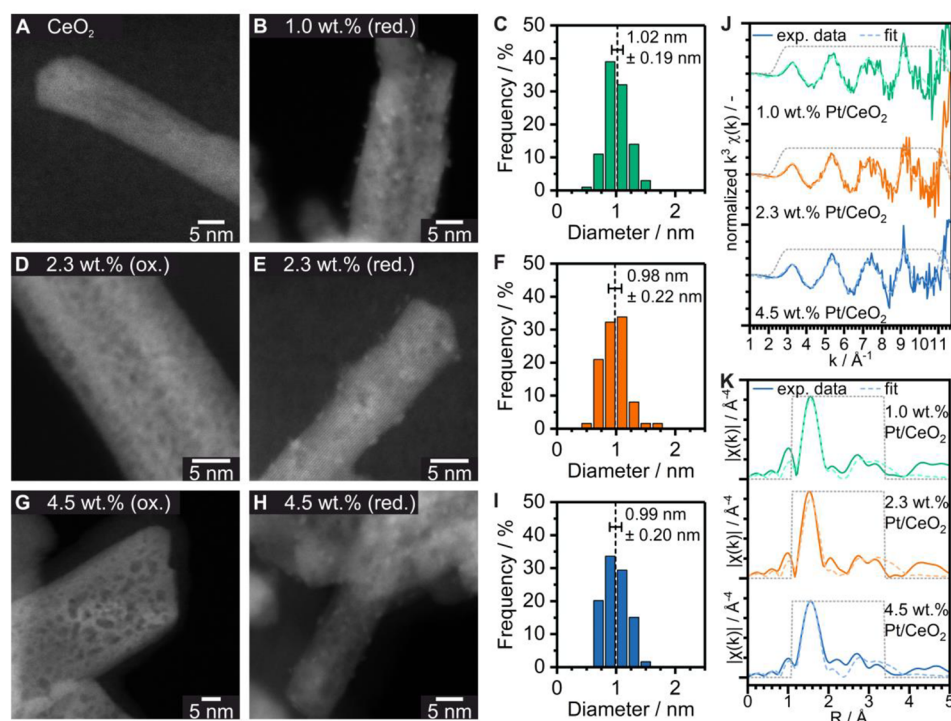
*Operando* XANES spectra were recorded at the P65 beamline (DESY, Hamburg, Germany).<sup>67</sup> The incoming X-ray beam was tuned in energy by a Si(111) DCM and had a size of 0.3 mm in height and 1.0 mm in width. Spectra were recorded in fluorescence mode using a silicon drift detector (SDD). 5.0 mg of the pressed and sieved ( $100\text{--}200 \mu\text{m}$ ) samples were placed in a quartz capillary reactor (1.0 mm outer diameter, 0.01 mm wall thickness). Heating, gas dosing, and gas analysis were conducted as described above. The heating rate was set to  $5 \text{ }^\circ\text{C min}^{-1}$  with a total flow of  $50 \text{ mL min}^{-1}$ . The reaction gas mixture contained 1000 ppm of CO and 10%  $\text{O}_2$  in He as balance gas. For the linear combination fitting, Pt foil recorded in transmission and the most oxidized sample spectrum (1.0 wt % Pt/CeO<sub>2</sub> in reaction mixture at room temperature) in fluorescence were used.

**2.8. Diffuse Reflectance Infrared Fourier Transform Spectroscopy.** Diffuse reflectance infrared Fourier transform spectroscopy (DRIFTS) measurements were performed on a Bruker Vertex 70 instrument with a Hg–Cd–Te (MCT) detector and a Praying Mantis high temperature reaction chamber with KBr windows. The cell temperature was controlled by two heating cartridges and a water cooling system inside the cell. As there is a strong temperature gradient,<sup>68,69</sup> the actual temperature of the catalyst bed was determined prior to the DRIFTS experiments by monitoring the bed temperature with an ImageIR 8300 camera (Infratec GmbH). The outlet gases were monitored using a Pfeiffer Vacuum OmniStar GSD 320 mass spectrometer (MS). The catalyst bed was prepared by filling part of the sample holder with  $\sim 100 \text{ mg}$  of  $\text{SiO}_2$  (sieve fraction  $125\text{--}150 \mu\text{m}$ ). On top, a layer of finely ground catalyst powder ( $\sim 30 \text{ mg}$ ) was placed. The gas stream was always kept at  $70 \text{ mL min}^{-1}$ . Before each measurement, the chamber was purged with Ar for 10 min before collecting the background spectra at room temperature (30 scans,  $4 \text{ cm}^{-1}$  resolution). Subsequently, the gas composition was switched to 1% CO/Ar, and spectra were recorded. The spectra were converted to a Kubelka–Munk unit using the OPUS software (Bruker).

**2.9. Density Functional Theory Calculations.** The density functional theory (DFT) calculations in this work were performed using the Vienna Ab Initio Simulation Package (VASP)<sup>70,71</sup> in connection with the Atomic Simulation Environment (ASE).<sup>72</sup> A plane-wave basis set with a cutoff energy of 450 eV, the projector augmented wave method (PAW),<sup>73,74</sup> and the Bayesian Error Estimation Functional with van der Waals correlations (BEEF-vdW)<sup>75</sup> were used. For a better description of localized Ce 4f electrons, the GGA+ $U$  ( $U =$

**Table 1. Results of ICP-OES Analysis and N<sub>2</sub> Physisorption, Specific Surface Area (SSA), Surface Noble Metal Concentration (SNMC), and Theoretical Fraction of a Pt Monolayer**

		low SNMC 1.0 wt % Pt/CeO <sub>2</sub>	medium SNMC 2.3 wt % Pt/CeO <sub>2</sub>	high SNMC 4.5 wt % Pt/CeO <sub>2</sub>
ICP-OES	Pt/wt %	1.03 ± 0.02	2.25 ± 0.05	4.49 ± 0.10
	Ce/wt %	75.4 ± 2.3	73.8 ± 2.2	71.7 ± 2.15
BET	SSA (after calcination)/m <sup>2</sup> g <sup>-1</sup>	59	68	73
	relative loss of the SSA compared to pure and uncalcined CeO <sub>2</sub> /%	36	26	21
Pt density	SNMC/mg m <sup>-2</sup>	17	33	62
	fraction of Pt monolayer/%	22.9	43.4	80.7

**Figure 2.** HAADF-STEM images of the Pt/CeO<sub>2</sub>-rods: CeO<sub>2</sub> nanorods (A), 2.3 wt % Pt/CeO<sub>2</sub> (D) and 4.5 wt % Pt/CeO<sub>2</sub> (G) after calcination at 600 °C for 5 h. No Pt entities were visible in the oxidized state. For the *ex situ* reduced catalysts, homogeneously distributed Pt particles were found for all catalysts with 1.0, 2.3, and 4.5 wt % Pt (B, E, H, respectively). The corresponding particle size distributions for the reduced catalysts (C, F, I) were determined after a treatment in hydrogen-containing atmosphere. The length of the CeO<sub>2</sub> nanorods was approximately 50–150 nm. For all three calcined samples, highly oxidized Pt species as clusters and single site species were found by EXAFS analysis (J, K).

5.0 eV) method<sup>76</sup> was applied. The choice of  $U$  is described in the SI. Three layers thick  $2 \times 2$  and  $3 \times 3$  large unit cells were used to represent CeO<sub>2</sub>(111) infinite slab models, each separated by more than 15 Å of vacuum in the  $z$  direction. These cell sizes were chosen to investigate the coverage effect on Pt migration. Diffusion barriers were calculated for entities of 1–4 Pt atoms on both  $2 \times 2$  and  $3 \times 3$  large unit cells of CeO<sub>2</sub>(111) using constrained optimizations (diffusion barriers, images as well as a detailed description of the optimization procedure is given in the SI). All atoms in the top layer of the CeO<sub>2</sub>(111) surface as well as the Pt clusters were allowed to relax during geometry optimizations. The Brillouin zones were sampled using  $(3 \times 3 \times 1)$  Monkhorst–Pack  $k$ -point grid<sup>77</sup> for  $2 \times 2$  and  $(2 \times 2 \times 1)$  for  $3 \times 3$  large unit cells. The convergence criterion for geometry optimizations was a maximum force of 0.01 eV/Å. Spin polarization was considered in all calculations.

### 3. RESULTS AND DISCUSSION

**3.1. Materials and *Ex Situ* Characterization.** The rod-shaped CeO<sub>2</sub> obtained by hydrothermal synthesis was found to have a specific surface area of 92 m<sup>2</sup> g<sup>-1</sup>. The support was loaded with three different Pt weight-loadings (1.0 wt % - low SNMC, 2.3 wt % - medium SNMC, and 4.5 wt % - high SNMC), leading to different Pt surface concentrations (23–81% of a monolayer, calculation following ref 38) and thus different interatomic distances of Pt species on the CeO<sub>2</sub> surface. To trigger the formation of highly dispersed and oxidized Pt species, all samples were calcined for 5 h at 600 °C in air,<sup>24,38</sup> which led to a certain decrease of the specific surface area (SSA) compared to the one of the bare CeO<sub>2</sub> before calcination (Table 1).

In agreement with previous studies, the highest Pt loading led to a less pronounced decrease in SSA upon calcination.<sup>43,78</sup> The samples after calcination in air are referred to as “oxidized”. As reference state, small, reduced Pt nanoparticles were generated by a reductive treatment (2% H<sub>2</sub>/N<sub>2</sub>, at 400 °C for 30 min, referred to as “reduced”) for all three samples.<sup>79</sup> Figure 2 depicts

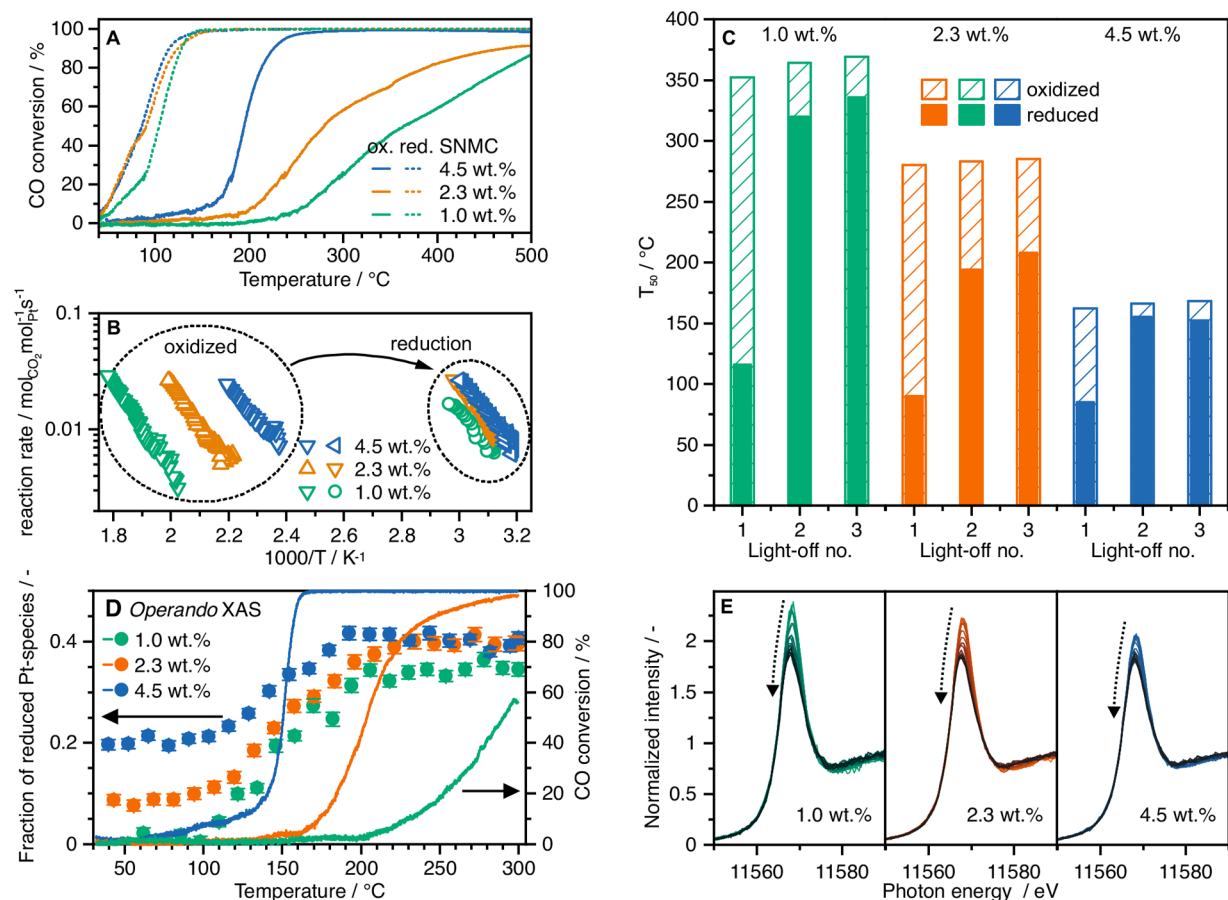


**Figure 3.** Transient ( $10\text{ }^{\circ}\text{C min}^{-1}$ ) CO oxidation activity (A) and Arrhenius plot (B) of Pt/CeO<sub>2</sub> with 1.0 wt % (green), 2.3 wt % (orange) and 4.5 wt % (blue) in oxidized (solid lines) and reduced (dashed lines) state (1000 ppm of CO, 10% O<sub>2</sub> in N<sub>2</sub>, WHSV: 60 000 L g<sub>Pt</sub><sup>-1</sup> h<sup>-1</sup>). The reproducibility of the catalytic activity and deactivation behavior were evaluated by comparing the temperature of 50% CO conversion  $T_{50}$  (C) in a series of light-offs. The oxidation state during CO conversion (D) was derived by linear combination fitting of *operando* XANES data (E). The arrow indicates the evolution of the XANES spectra with increasing temperature

**Table 2.** Activation Energy  $E_A$  Derived from the Arrhenius Plot in Figure 3 and  $T_{50}$  (1000 ppm of CO, 10% O<sub>2</sub> in N<sub>2</sub>, WHSV: 60 000 L g<sub>Pt</sub><sup>-1</sup> h<sup>-1</sup>) for the Oxidized and Reduced 1.0–4.5 wt % Pt/CeO<sub>2</sub> Samples

		low SNMC 1.0 wt % Pt/CeO <sub>2</sub>	medium SNMC 2.3 wt % Pt/CeO <sub>2</sub>	high SNMC 4.5 wt % Pt/CeO <sub>2</sub>
$E_A$	oxidized/kJ mol <sup>-1</sup>	67.7 ± 0.6	70.2 ± 0.9	60.2 ± 0.9
	reduced/kJ mol <sup>-1</sup>	31.8 ± 0.3	62.5 ± 0.6	57.1 ± 0.7
$T_{50}$	oxidized/°C	365	282	195
	reduced/°C	103	90	86

the HAADF-STEM images collected to reveal the microstructures of pure CeO<sub>2</sub> support as well as the oxidized and reduced Pt/CeO<sub>2</sub> catalysts. The CeO<sub>2</sub> support showed a rod-shape with an average diameter of the particles around 20 nm. For the oxidized catalysts, no Pt entities were visible on the CeO<sub>2</sub> nanorods (Figure 2D,G). This is in line with previous observation that an oxidizing treatment above 400 °C leads to the formation of highly dispersed Pt species.<sup>24</sup> EXAFS analysis of the oxidized catalysts (Pt L<sub>3</sub>-edge; Figure 2J,K) indicated the presence of atomically dispersed Pt-species in CeO<sub>2</sub>-hollow sites as well as PtO<sub>x</sub>-clusters (cf. SI) for all three SNMCs. This additionally confirmed the oxidized and highly dispersed state of Pt species in all investigated catalysts. After the reductive treatment, Pt nanoparticles with an average particle size of ca. 1 nm on CeO<sub>2</sub> were observed for all samples (Figure 2C,F,I). The HAADF-STEM images were analyzed using Delaunay triangulation to determine an average distance between the formed

nanoparticles (Figure S11 and Table S6). The results showed that, indeed, the average distance decreases with rising SNMC. This indicates just a trend since the STEM images are only two-dimensional projection of a three-dimensional object.

**3.2. Trends in Catalytic Activity.** By normalizing the amount of catalyst in the catalytic reactor to the Pt loading, a direct comparison of the CO oxidation activity was possible for the three Pt/CeO<sub>2</sub> samples despite of the differences in Pt weight loadings. In contrast to the *ex situ* characterization results, the CO light-off tests of the oxidized catalysts revealed striking differences between the catalytic activity, scaling strongly with the SNMC (Figure 3A).

The temperature values at 50% CO conversion ( $T_{50}$ ) were 352 °C, 280 °C, and 162 °C for the samples containing 1.0, 2.3, and 4.5 wt % Pt, respectively. This trend aligns well with the increase of SNMC. The catalyst with the lowest SNMC barely reached full conversion even at 500 °C. The here observed

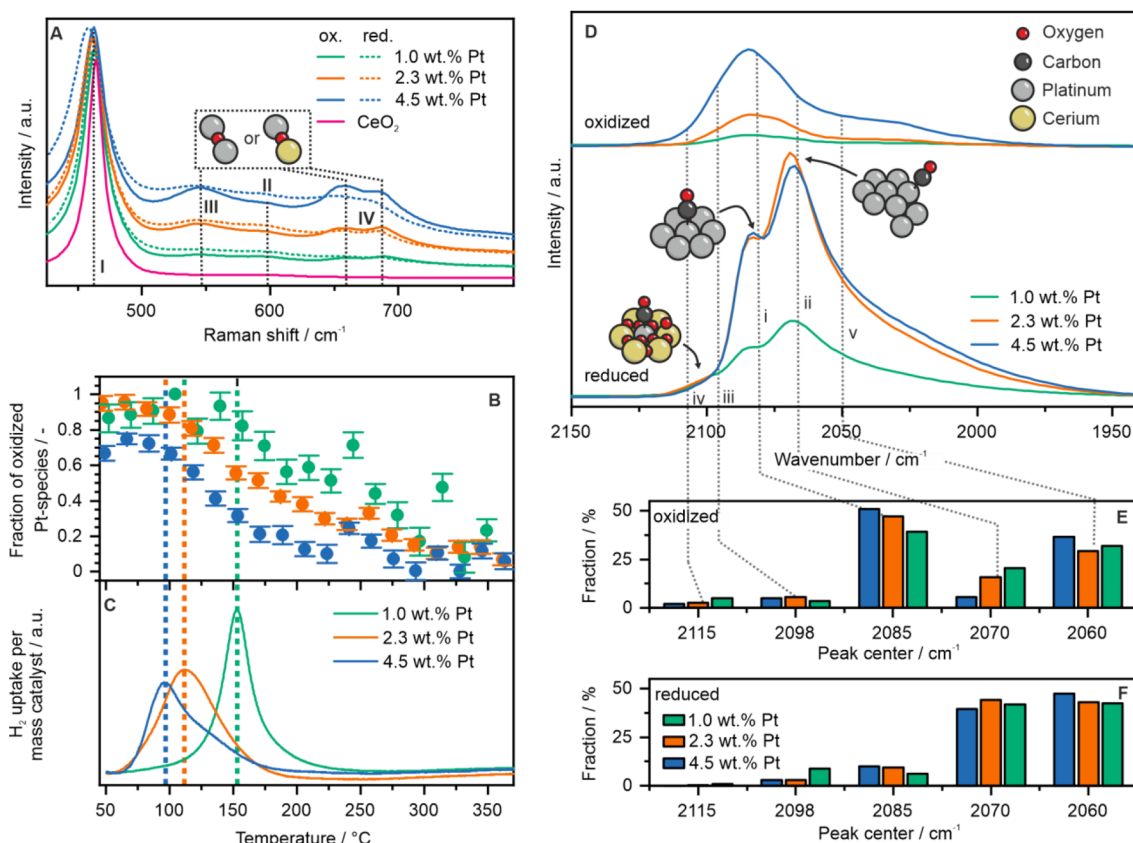


**Figure 4.** Raman spectra of  $\text{CeO}_2$  and the oxidized and reduced Pt/ $\text{CeO}_2$  samples (A). Linear combination analysis of the Pt  $L_{3\text{-edge}}$  XAS spectra during TPR in  $\text{H}_2$  of as-prepared samples (B).  $\text{H}_2$ -TPR experiments using a TCD (C). *In situ* DRIFTS results (D, the adsorption geometry of CO is indicated in insets with gray spheres representing Pt, yellow Ce, red O, and black C) and the peak ratio of the oxidized (E) and reduced (F) Pt/ $\text{CeO}_2$  catalysts.

tendency in catalytic activity is in line with the trend illustrated in Figure 1 for previously investigated Pt/ $\text{CeO}_2$  catalysts: a high surface concentration of Pt correlates to a higher activity. The corresponding reaction rates derived from the light-off experiment are depicted in Figure 3B. The activation energies (Table 2) for the oxidized catalysts are between 60 and 70  $\text{kJ mol}^{-1}$ , matching with reported values in literature.<sup>59</sup>

All catalysts became more active after a reduction pretreatment (2%  $\text{H}_2$  at 400 °C for 30 min), which shifted the  $T_{50}$  temperature to 116 °C, 90 °C, and 85 °C with increasing SNMC, respectively. In contrast to the oxidized samples, the catalytic activity for both medium and highly Pt loaded samples was almost identical upon reduction. Only the low SNMC sample differed slightly in slope and shape of the light-off curve, resulting in a 25–30 °C higher  $T_{50}$ . The activation energies (Table 2) for the reduced catalysts are 32–63  $\text{kJ mol}^{-1}$  (in good agreement with other studies for prior reduced Pt/ $\text{CeO}_2$  catalysts<sup>51,80</sup> reporting values of 42–51  $\text{kJ mol}^{-1}$ ). Also, for the reduced samples, three consecutive light-off tests to 500 °C were performed. A light-off to 500 °C leads to full conversion at temperatures above 200 °C; hence, the majority of the catalyst bed is only exposed to carbon dioxide and oxygen. These mainly oxidizing conditions are similar to the pretreatment of the oxidized catalysts. Hence, each light-off showed a decrease in catalytic activity (Figure 3C), with the last CO oxidation light-off of this series comparable to the activity of the oxidized catalysts, including the pronounced differences in activity. It is apparent that at high temperatures, the SNMC also strongly

influences the catalyst stability and that the activation in hydrogen is reversed by a high temperature light-off.

To investigate the oxidation state of Pt, we performed *operando* XANES experiments at the Pt  $L_{3\text{-edge}}$ . The online gas analysis during the light-off experiments confirmed the strong differences in catalytic activity (Figure 3D, solid lines). The simultaneous monitoring of the Pt oxidation state using a linear combination fitting (LCF) of the spectra showed that the noble metal state changes as soon as it is exposed to lean CO oxidation conditions at room temperature. This is indicated by a distinct decrease of the so-called white line compared to the as-prepared catalysts in air, where only minor differences between the three SNMC samples were observed (Figure S5A). The catalyst with a high SNMC tends to reduce stronger than that with a medium SNMC, while the low SNMC sample remains completely oxidized. During temperature increase, a reduction of Pt was observed for all catalysts with an onset at 100–150 °C. For the sample with a high SNMC, the start of Pt reduction coincides with the sharp CO oxidation light-off. However, for the two other catalysts, the reduction of the noble metal seems to be decoupled from the light-off which happens at higher temperatures. At around 200 °C, all catalysts reach a similar oxidation state for Pt, which can be fitted by a 40% mixture of  $\text{Pt}^0$  and 60%  $\text{Pt}^{4+}$  reference component. A further speciation into clusters, monatomic Pt, or nanoparticles is not possible on the basis of XANES alone. Therefore, in order to identify the descriptors for this behavior of the differently loaded Pt/ $\text{CeO}_2$  catalysts, the noble metal reducibility and CO adsorption properties were

studied by complementary Raman spectroscopy, *in situ* XAS, and DRIFTS.

**3.3. In-Depth Characterization of the Pt-CeO<sub>2</sub> Interaction.** The vibrational modes detected by Raman spectroscopy (Figure 4A) are sensitive to the presence of defects in the CeO<sub>2</sub> structure and the binding properties of Pt to the support.<sup>81</sup> For all catalysts, Raman bands appear at 457, 548, 595, 658, and 687 cm<sup>-1</sup>. The band at 457 cm<sup>-1</sup> (I) is characteristic for the I<sub>F2g</sub> symmetric stretch mode of CeO<sub>2</sub>.<sup>82,83</sup> The defect-related I<sub>D</sub> mode of CeO<sub>2</sub> at 595 cm<sup>-1</sup> (II) is caused by a displacement of an oxygen ion from its lattice position to an interstitial position leaving a vacancy at its genuine lattice position.<sup>84</sup> Raman bands around 550 cm<sup>-1</sup> (III) and 665–690 cm<sup>-1</sup> (IV) are assigned to Pt-O species.<sup>78,81,85,86</sup> They are characteristic features of Pt/CeO<sub>2</sub> materials (Pt-O species in close or direct vicinity to CeO<sub>2</sub>) and are not observed for pure PtO<sub>x</sub><sup>84</sup> or PtO<sub>x</sub>/Al<sub>2</sub>O<sub>3</sub> (Figure S3). Mapping of these bands normalized to the intensity of the defect CeO<sub>2</sub>-I<sub>D</sub> mode shows a spatial correlation of CeO<sub>2</sub> defects with Pt-O species (Figure S4).

The relative intensity of detected Pt-O(-Ce) bands increased with the noble metal concentration on the surface of ceria (rise of bands at 550 cm<sup>-1</sup> and 665–690 cm<sup>-1</sup>). Interestingly, the Pt-O(-Ce) feature at 665–690 cm<sup>-1</sup> exhibits two distinctive Raman bands, which change their ratio with increasing SNMC and alteration of the Pt–O bond nature. In addition, the defect concentration in CeO<sub>2</sub> rises with Pt loading (broadening of the 457 cm<sup>-1</sup> band<sup>82,83</sup> and increase of the CeO<sub>2</sub>-I<sub>D</sub> band). Upon reduction, the features attributed to oxidic Pt species diminished, but the higher defect concentration on ceria surface for increasing noble metal loadings remained.

The strength and scission of Ce–O and Pt–O bonds were found to be directly linked to the reduction behavior of the catalyst. Figure 4B reports the results of the H<sub>2</sub>-TPR monitored by *in situ* XAS at the Pt L<sub>3</sub>-edge (corresponding normalized spectra, Figure S5 B–D). A trend in Pt reduction temperature following the SNMC was observed for the three oxidized catalysts with the high SNMC Pt/CeO<sub>2</sub> catalyst reducing at the lowest temperature (~130 °C) followed by the medium (~170 °C) and low SNMC (~220 °C). This is in line with the *operando* XANES data collected during CO oxidation for the three catalysts (Figure 3D). Additionally, hydrogen consumption determined during a H<sub>2</sub>-TPR probed the temperature-dependent reducibility of the support material (Figure 4C). The sample with the highest SNMC showed the peak maximum at the lowest temperature of 96 °C, followed by the medium SNMC (111 °C) and the low SNMC (153 °C). The temperature of maximum H<sub>2</sub> consumption also follows the trends observed during the XAS experiments. Yet, the amount of consumed H<sub>2</sub> appears not to be correlated to the SNMC.

The characterization methods above support the hypothesis that the noble metal concentration on the CeO<sub>2</sub> surface of the oxidized catalysts strongly affects CO oxidation activity as well as the Pt and CeO<sub>2</sub> reducibility. These differences were not indicated by the EXAFS analysis because the Pt species exhibited similar structural characteristics in all as-prepared catalysts (Figure 2). The use of CO as a probe molecule in DRIFTS measurements provides complementary information on the local noble metal surface structure.<sup>41,87,88</sup> Figure 4D shows the IR spectra of the CO adsorbed (1% CO/Ar) samples at room temperature in the reduced and oxidized states. The vibrational modes of CO adsorbed on Pt give rise to peaks in the wavenumber range between 1950 and 2100 cm<sup>-1</sup>. For all reduced catalysts, two significant features at 2069 and 2086 cm<sup>-1</sup>

were observed. Furthermore, a small shoulder around 2096 cm<sup>-1</sup> was found. Compared with the reduced catalysts, the IR band intensity for the calcined samples was lower (approximately by a factor of 2) indicating that part of the sites were not able to serve as host sites because of their unfavorable adsorption geometry.<sup>38,45</sup> Furthermore, the oxidized catalysts showed a strong dependence of the overall signal intensity on the SNMC. Most notably, the intensity in the Kubelka–Munk plot recorded for the 4.5 wt % Pt/CeO<sub>2</sub> catalyst is 6.8 times higher than that of the 1.0 wt % Pt/CeO<sub>2</sub> sample. For all oxidized catalysts, the bands are shifted to higher wavenumbers. The ratio of the peaks at 2085 and 2070 cm<sup>-1</sup> changed with the latter being more pronounced compared with the reduced state.

On the basis of these qualitative observations, the spectra were deconvoluted<sup>87,89</sup> into Gaussian peaks (Figure 4E,F). The respective peak position provides information on the nature of Pt species, on which CO is adsorbed. The peak at ~2086 cm<sup>-1</sup> (Figure 4D; (i) can be assigned to CO linearly adsorbed on Pt<sup>0</sup> terrace sites, which are present on slightly larger Pt NPs.<sup>90</sup> Lower wavenumbers are referred to CO linearly adsorbed on lower coordinated Pt atoms (e.g., step sites and edge sites), which correspond to subnanometer Pt NPs.<sup>90</sup> Therein, a peak around ~2070 cm<sup>-1</sup> (ii) can be traced back to kink site Pt atoms of a Pt NP.<sup>91</sup> The band at 2096 cm<sup>-1</sup> (iii) was previously assigned to CO adsorbed on single Pt sites.<sup>41,92</sup> Recent studies<sup>45,93</sup> contradict this assignment and attribute this band to oxidic clusters. As the Pt/CeO<sub>2</sub> system was shown to be highly dynamic, these clusters could be present in the as-prepared catalysts or could form *in situ* under reducing conditions. Such behavior was observed already in a previous study,<sup>38</sup> where this band was absent at low temperatures (around 170 K) and appeared upon exposure to higher CO concentrations already at room temperature.<sup>38</sup> Despite the ambiguities in the assignment of this band, it can be stated that this feature indicates highly oxidized and dispersed Pt species - whether single sites or clusters. Vibrational bands above 2100 cm<sup>-1</sup> (iv) are generally reported for CO adsorbed on PtO<sub>x</sub>. Toward lower wavenumbers, features at 2060 cm<sup>-1</sup> and below (v) can be attributed to CO–CO interactions which increase with CO coverage of the Pt surface. In the case of partially oxidized Pt species, those peaks are shifted to higher wavenumbers.

The peak deconvolution<sup>87,89</sup> in the case of the reduced Pt/CeO<sub>2</sub> catalysts (Figure 4F) revealed very similar ratios of edge, corner, terrace, or single sites for all three catalysts. The state and particle size of Pt seem to be nearly identical after reduction regardless of the SNMC, which is in line with the catalytic activity and findings of the *ex situ* characterization (Raman spectroscopy, TEM). In contrast, the oxidized samples show a trend in terms of peak ratios depending on the Pt surface concentration (Figure 4E). The Pt loading on ceria surface seems to play a major role. At a higher SNMC, more CO was adsorbed on Pt terrace sites than on Pt corners showing that larger particles<sup>87,89</sup> were formed with increasing SNMC. Interestingly, the peak position suggests the presence of Pt<sup>0</sup> rather than the pure presence of oxidized Pt as suggested by XAS. Under the applied measurement conditions (25 °C, 1% CO/Ar), changes of the sample structure can be induced,<sup>38,94</sup> such as the formation of small clusters via the reduction of isolated Pt species. This is in line with the TPR and Raman spectroscopy results: A higher SNMCs favors the formation of clusters/particles.

A critical factor for such a Pt agglomeration process is the mobility of Pt species, especially that of highly dispersed single

atoms or clusters, on the CeO<sub>2</sub> surface. In order to investigate how Pt species migrate on ceria to form larger clusters and particles, and thus to substantiate the trends observed above, the diffusion barriers of isolated Pt atoms and small Pt clusters up to the size of four Pt atoms have been calculated (Table 3) using

**Table 3. Diffusion Barriers for Pt Single Sites to 4-Atom Pt Clusters on a 2 × 2 and 3 × 3 CeO<sub>2</sub> (111) Surface Unit Cell Calculated by DFT (GGA+U)**

number of Pt atoms in the unit cell	diffusion barrier of Pt species on a 2 × 2 CeO <sub>2</sub> unit cell/kJ mol <sup>-1</sup>	diffusion barrier of Pt species on a 3 × 3 CeO <sub>2</sub> unit cell/kJ mol <sup>-1</sup>
1	70	90
2	42	64
3	79	97
4	116	138

density functional theory (DFT). All calculations were performed for the CeO<sub>2</sub>{111} facet, which is thermodynamically favored at higher temperatures,<sup>38</sup> covered with Pt entities at different distances. The diffusion barriers were calculated for two different SNMC. Small (7.7 Å) interatomic distances were used to mimic the medium SNMC in this study, whereas larger interatomic distances (11.6 Å) achieved by varying the unit cell were applied for the low SNMC sample. Hereby, larger distances, which equal lower SNMC, exhibit higher diffusion barriers (cf. Figures S6–S9). As can be seen in Table 3, Pt single atoms have comparatively low diffusion barriers of 70 and 90 kJ mol<sup>-1</sup> depending on their distance. These barriers increase by 40–50 kJ mol<sup>-1</sup> when increasing the Pt cluster size to 4, the largest considered herein. We note that high diffusion barriers for larger noble metal clusters were also seen in previous studies in temperature ranges up to 900 °C.<sup>95</sup>

We thus speculate that the cluster/particle formation is mainly related to the diffusivity of smaller Pt entities, while larger clusters and particles are less mobile. Using a barrier of 90 kJ mol<sup>-1</sup> for the larger 3 × 3 CeO<sub>2</sub> (111) unit cell model and 70 kJ mol<sup>-1</sup> for the 2 × 2 CeO<sub>2</sub> (111) unit cell model, the diffusion constants can be furthermore estimated using the following equation:<sup>96</sup>

$$D = \frac{l^2 k_B T}{h} e^{-E_A/k_B T}$$

Here,  $l$  represents the interatomic distance between two Pt entities,  $k_B$  is the Boltzmann constant, and  $h$  the Planck constant. As the diffusion constant decreases with increasing activation barrier  $E_A$ , the Pt entities in the smaller unit cell are generally more mobile than in the larger one. Thus, a higher concentration of Pt single atoms requires a lower activation temperature as the distances between atoms and clusters are smaller. When comparing the diffusion constant for single atom species in the small (70 kJ mol<sup>-1</sup>) and large (90 kJ mol<sup>-1</sup>) unit cell depending on the temperature to the CO conversion for the 1.0 and 2.3 wt % Pt/CeO<sub>2</sub> catalyst, a striking trend can be observed (Figure 5). The difference in catalytic activity due to the 1.9 times higher SNMC (cf. Figure 3) is reflected very well by the calculated diffusion constants at low conversions. Thus, the formation of clusters and small particles in highly oxidized and dispersed Pt/CeO<sub>2</sub> samples as the limiting step for the CO conversion can be directly deduced. This is in line with our observations from catalytic testing and corresponding characterization data.

**3.4. Implications Resulting from the Evolution of the Pt Structure under Reaction Conditions.** The ongoing research on Pt/CeO<sub>2</sub> catalysts revealed that several different Pt species can be present on the support surface. Their characterization is difficult considering the limited insights which the currently available toolset provides.<sup>97</sup> Further complications arise because of the dynamic nature<sup>24,38</sup> of the catalyst under reaction conditions, as also revealed in this work. In order to gain a fundamental understanding, efforts are invested in the synthesis of catalysts containing uniform Pt species, which is generally easier to achieve at low weight loadings.<sup>45,98</sup> Considering our observations, we suggest the model as illustrated in Scheme 1 for the Pt/CeO<sub>2</sub> catalyst series with different Pt loadings: For ceria-based catalysts, homogeneous and highly distributed species (i.e., single sites or small clusters) can be obtained also by treatments at elevated temperature, as applied in this study. As illustrated by the STEM images as well as XAS and DRIFTS measurements, in all as-prepared catalysts Pt is present as highly dispersed and oxidized species (i.e., single sites and clusters). Noble metal particles of approximately 1 nm

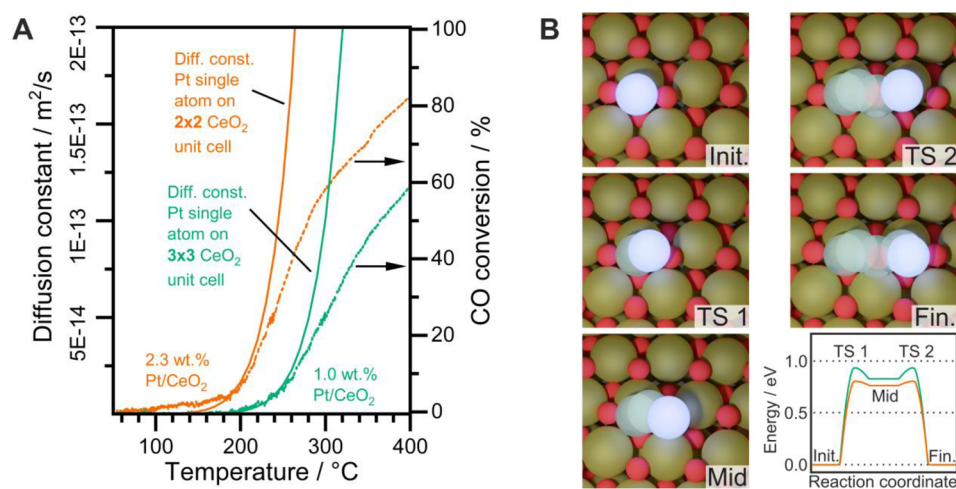
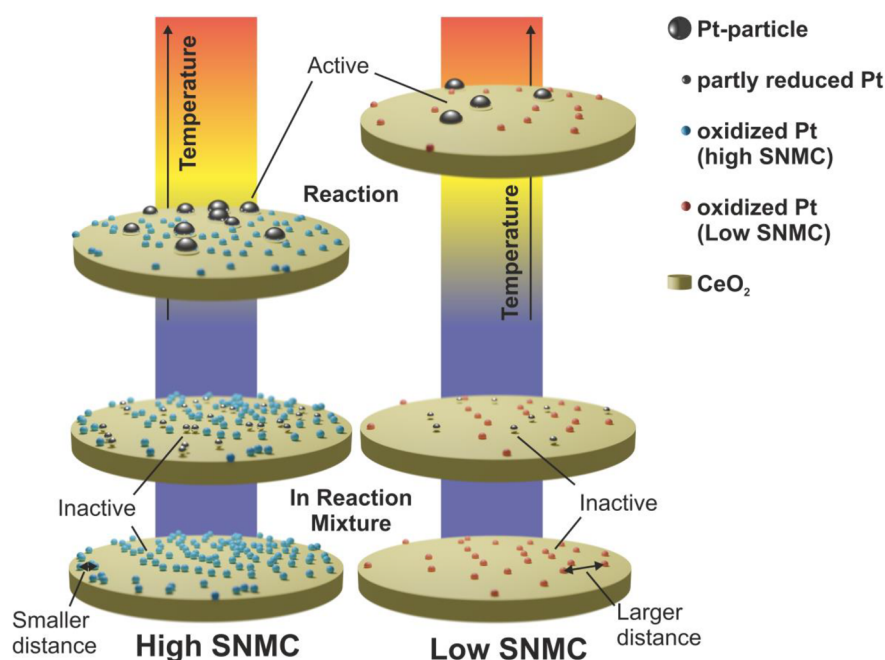


**Figure 5.** Comparison of the diffusion barrier for Pt single sites supported on a 3 × 3 CeO<sub>2</sub> (111) unit cell and supported on a 2 × 2 CeO<sub>2</sub> (111) unit cell with the catalytic CO conversion curves of the 1.0 and 2.3 wt % Pt/CeO<sub>2</sub> samples after calcination (A). Visualization of the diffusion path of a single atom over the CeO<sub>2</sub> (111) surface with diffusion energy diagram (B); for more details, see Figures S6–S9).



**Scheme 1. Proposed Model on the Cluster Formation under Reaction Conditions and Resulting Catalytic Activity Depending on the SNMC<sup>a</sup>**



<sup>a</sup>Below the corresponding ignition temperature, the Pt species are present mostly as oxidized single-atomically dispersed species, which can partly reduce under reaction conditions. While a low SNMC leads to high interspecies distances and thus high temperatures to form catalytically active clusters, a higher SNMC enhances the low temperature activity by increasing the probability of cluster formation under reaction conditions. Therefore, the SNMC has a strong influence on the corresponding CO oxidation activity.

are formed only after reduction at 400 °C in hydrogen containing atmosphere.

Regarding their activity for CO oxidation, the majority of Pt species might inherit varying degrees of catalytic activity depending on the temperature range and reaction conditions. However, previous studies have shown that a too strong stabilization by the support is disadvantageous for oxidation reactions.<sup>38,78,99</sup> This was also confirmed in the present investigation when comparing the reduced samples with the as-prepared ones. Only a very low conversion was observed for the calcined 1.0–4.5 wt % Pt catalyst materials below the ignition of CO oxidation, which could be due to a small amount of remaining PtO<sub>x</sub> clusters that are activated by CO during the reaction onset (as observed in the *operando* XAS experiment Figure 3D,E). Despite the probability to have such small clusters is higher for the highly loaded Pt/CeO<sub>2</sub> catalyst, this seems not sufficient to obtain a considerable CO conversion activity below 150 °C (cf. Figure 3A). In line with the results reported in ref 43, a minor impact of the SNMC was observed in this temperature range corresponding to a rather “immobile” Pt state. In contrast, the sharp ignition of the CO oxidation above 150 °C suggest further changes in Pt structure. According to the *operando* XAS data, the increase of temperature leads to further reduction of Pt species. Nonetheless, as demonstrated in our previous study,<sup>38</sup> isolated single atoms or highly dispersed species are not active even if partially reduced, and contribute notably to CO oxidation only if the reaction temperature sustains their migration with formation of larger clusters.<sup>38</sup>

By breaking the bonds with the support material at higher temperatures, Pt species become more mobile and diffuse over the CeO<sub>2</sub> surface. For the catalyst with low SNMC, most Pt sites have a large average interspecies distance. This long distance

requires higher temperatures to promote the migration and formation of larger clusters, as supported by DFT calculations revealing the increase in diffusion barrier with larger interatomic distances (Table 3). By increasing the concentration of the noble metal on the ceria surface, and thus decreasing the interspecies distance, the probability for the mobile species to find each other and agglomerate to reduced particles/clusters is enhanced. These agglomerates are then active for the CO oxidation.

At the other end of the scale, an “upper” limit of catalyst loading exists above a monolayer, where an anchoring of individual noble metal atoms is not anymore possible and Pt particles become stable even at high temperature and under oxidizing atmospheres.<sup>46,95</sup>

As a certain Pt cluster size is necessary for the onset of the CO oxidation,<sup>44</sup> the catalyst with the highest SNMC requires the lowest temperatures to become active. A reductive treatment anticipates the dynamic Pt particle formation and thus yields very active catalysts. These Pt particles show CO oxidation activity almost independent of the SNMC. Thus, the SNMC seems to be the main influencing factor during the *in situ* cluster/particle or active site formation.

As a consequence of these findings, four observations are highlighted:

- (1) This study shows that the concentration of Pt on ceria surface must be high enough to favor the formation of clusters and particles, which are known to sustain oxidation reactions. A high surface noble metal concentration is furthermore a potential key to prevent catalyst deactivation due to a too strong redispersion at elevated reaction temperatures.

- (2) In order to design an efficient Pt/CeO<sub>2</sub> catalyst, an optimal SNMC needs to be found with the focus not only on activity but also on possible sintering events. More precisely, the interatomic distance between Pt species should not be too small and thus the SNMC not too high to circumvent sintering of Pt.<sup>100</sup> Considering aspects 1 and 2 will allow optimizing the economy of the scarce and expensive noble metals in catalysis in a knowledge-based manner.
- (3) If the catalytic and chemical properties of Pt/CeO<sub>2</sub> catalysts are compared, the loading has to be normalized to the CeO<sub>2</sub> surface to ensure a similar SNMC.
- (4) To maintain a reasonable cost for such noble metal based catalysts, the SNMC could be adjusted on the expense of ceria surface area decrease or the addition of a less interacting support like Al<sub>2</sub>O<sub>3</sub> and not on the increase of the noble metal loading.

#### 4. CONCLUSION

By systematically varying the surface noble metal concentration of a well-defined Pt/CeO<sub>2</sub> catalyst, we found that the chemical and catalytic properties of the oxidized catalysts are strongly correlated to this descriptor. Our investigations demonstrated that the tendency to form Pt clusters/particles increases when the Pt interspecies distance is decreased, as identified by Raman spectroscopy, XAS and DRIFTS measurements. Additionally, the promotion of Pt species migration at high SNMC was substantiated by DFT calculations, which show that the diffusion barrier for Pt single sites and up to 4-atom clusters decreases, if the interatomic distance diminishes. In consequence, the catalytic properties of supported noble-metal-based catalysts during the CO oxidation, and probably other related reactions, strongly depend on the SNMC because of the formation of larger clusters and facilitated mobility. A low surface concentration of Pt leads to a large fraction of sparsely anchored single Pt atoms, which require high temperatures to reduce and migrate for generating the catalytically active Pt clusters or nanoparticles. Increasing the SNMC leads to smaller average distances between the Pt species and possibly also to the formation of oxidized Pt-clusters that are activated at much lower temperatures. Therefore, the SNMC is a key descriptor for the low temperature activity of Pt/CeO<sub>2</sub> catalysts, which has a strong influence on the fate and stability of the noble metal species. Our study shows that this parameter should be considered for future catalyst synthesis in the large application field of noble-metal-catalyzed oxidation and hydrogenation reactions, in which an optimal noble metal structure is essential for resource efficient use of the scarce material.

#### ■ ASSOCIATED CONTENT

##### SI Supporting Information

The Supporting Information is available free of charge at <https://pubs.acs.org/doi/10.1021/acscatal.1c04565>.

Additional information on the EXAFS data evaluation including structural models, EXAFS data analysis, Raman spectra and mapping as well as the XANES data during temperature-programmed reduction and diffusion energy diagrams received by DFT investigations (PDF)

All structures of the VASP calculations are summarized as CONTCAR files (TXT)

#### ■ AUTHOR INFORMATION

##### Corresponding Author

**Jan-Dierk Grunwaldt** – Institute for Chemical Technology and Polymer Chemistry (ITCP), Karlsruhe Institute of Technology (KIT), 76131 Karlsruhe, Germany; Institute of Catalysis Research and Technology (IKFT), Karlsruhe Institute of Technology (KIT), 76344 Eggenstein-Leopoldshafen, Germany; [orcid.org/0000-0003-3606-0956](https://orcid.org/0000-0003-3606-0956); Email: [grunwaldt@kit.edu](mailto:grunwaldt@kit.edu)

##### Authors

**Florian Maurer** – Institute for Chemical Technology and Polymer Chemistry (ITCP), Karlsruhe Institute of Technology (KIT), 76131 Karlsruhe, Germany; [orcid.org/0000-0002-3307-4132](https://orcid.org/0000-0002-3307-4132)

**Arik Beck** – Institute for Chemical Technology and Polymer Chemistry (ITCP), Karlsruhe Institute of Technology (KIT), 76131 Karlsruhe, Germany; Present Address: A.B.: ETH Zurich, Vladimir-Prelog-Weg 1-5/10, 8093 Zürich, Switzerland; [orcid.org/0000-0001-5267-3141](https://orcid.org/0000-0001-5267-3141)

**Jelena Jelic** – Institute of Catalysis Research and Technology (IKFT), Karlsruhe Institute of Technology (KIT), 76344 Eggenstein-Leopoldshafen, Germany

**Wu Wang** – Institute of Nanotechnology (INT), Karlsruhe Institute of Technology (KIT), 76344 Eggenstein-Leopoldshafen, Germany; Present Address: W.W.: Department of Physics, Southern University of Science and Technology, 518055 Shenzhen, China

**Stefan Mangold** – Institute for Photon Science and Synchrotron Radiation (IPS), Karlsruhe Institute of Technology (KIT), 76344 Eggenstein-Leopoldshafen, Germany

**Matthias Stehle** – Institute for Chemical Technology and Polymer Chemistry (ITCP), Karlsruhe Institute of Technology (KIT), 76131 Karlsruhe, Germany; [orcid.org/0000-0002-7382-5666](https://orcid.org/0000-0002-7382-5666)

**Di Wang** – Institute of Nanotechnology (INT), Karlsruhe Institute of Technology (KIT), 76344 Eggenstein-Leopoldshafen, Germany; [orcid.org/0000-0001-9817-7047](https://orcid.org/0000-0001-9817-7047)

**Paolo Dolcet** – Institute for Chemical Technology and Polymer Chemistry (ITCP), Karlsruhe Institute of Technology (KIT), 76131 Karlsruhe, Germany; [orcid.org/0000-0001-9583-9375](https://orcid.org/0000-0001-9583-9375)

**Andreas M. Gänzler** – Institute for Chemical Technology and Polymer Chemistry (ITCP), Karlsruhe Institute of Technology (KIT), 76131 Karlsruhe, Germany

**Christian Kübel** – Institute of Nanotechnology (INT), Karlsruhe Institute of Technology (KIT), 76344 Eggenstein-Leopoldshafen, Germany; [orcid.org/0000-0001-5701-4006](https://orcid.org/0000-0001-5701-4006)

**Felix Studt** – Institute for Chemical Technology and Polymer Chemistry (ITCP), Karlsruhe Institute of Technology (KIT), 76131 Karlsruhe, Germany; Institute of Catalysis Research and Technology (IKFT), Karlsruhe Institute of Technology (KIT), 76344 Eggenstein-Leopoldshafen, Germany; [orcid.org/0000-0001-6841-4232](https://orcid.org/0000-0001-6841-4232)

**Maria Casapu** – Institute for Chemical Technology and Polymer Chemistry (ITCP), Karlsruhe Institute of Technology (KIT), 76131 Karlsruhe, Germany; [orcid.org/0000-0002-8755-9856](https://orcid.org/0000-0002-8755-9856)

Complete contact information is available at: <https://pubs.acs.org/doi/10.1021/acscatal.1c04565>

## Author Contributions

#F.M. and A.B. contributed equally.

## Notes

The authors declare no competing financial interest.

## ACKNOWLEDGMENTS

F.M. acknowledges the “Fonds der Chemischen Industrie” (FCI) of the Verband der Chemischen Industrie e.V. (VCI) for financial support during his Ph.D. studies. The state of Baden-Württemberg is thanked by J.J. and F.S. for its support through bwHPC (bwunicluster and JUSTUS, RV bw16G001 and bw17D011). This study was further funded by the Deutsche Forschungsgemeinschaft (DFG, German Research Foundation) – SFB 1441 – Project-ID 426888090 (projects B2, B3, B4). The DFG is also thanked for financial support of the infrastructure at KIT (INST 121384/16-1, INST 121384/73-1). Furthermore, the German Federal Ministry for Economic Affairs and Energy (BMWi: 19U15014B) and the French National Research Agency (ANR-14-CE22-0011-02) are acknowledged for funding of the DEUFRAKO collaboration ORCA. The authors thank the KIT light source for beamtime at the CAT-ACT and XAS beamlines. We acknowledge DESY (Hamburg, Germany), a member of the Helmholtz Association HGF, for the provision of experimental facilities. Electron microscopy was supported by the Karlsruhe Nano Micro Facility (KNMF), a Helmholtz Research Infrastructure at KIT. Parts of this research were carried out at PETRA III and we would like to thank E. Welter and R. Biller for assistance in using the photon beamline P65. Beamtime was allocated for the proposal I-20210886. We thank A. Zimina (IKFT, KIT) for the measurements of the *ex situ* samples and D. Zengel and M. Eck (ITCP, KIT) for their assistance during the *in situ* XAS experiments. T. Bergfeldt (IAM-AWP, KIT) is acknowledged for ICP-OES analysis.

## REFERENCES

- (1) Zhang, L.; Zhou, M.; Wang, A.; Zhang, T. Selective Hydrogenation over Supported Metal Catalysts: From Nanoparticles to Single Atoms. *Chem. Rev.* **2020**, *120* (2), 683–733.
- (2) Liu, L.; Corma, A. Metal Catalysts for Heterogeneous Catalysis: From Single Atoms to Nanoclusters and Nanoparticles. *Chem. Rev.* **2018**, *118* (10), 4981–5079.
- (3) Kalz, K. F.; Kraehnert, R.; Dvovashkin, M.; Dittmeyer, R.; Glaeser, R.; Krewer, U.; Reuter, K.; Grunwaldt, J.-D. Future Challenges in Heterogeneous Catalysis: Understanding Catalysts under Dynamic Reaction Conditions. *ChemCatChem*. **2017**, *9* (1), 17–29.
- (4) Lott, P.; Deutschmann, O. Lean-Burn Natural Gas Engines: Challenges and Concepts for an Efficient Exhaust Gas Aftertreatment System. *Emiss. Control Sci. Technol.* **2021**, *7* (1), 1–6.
- (5) Bernal, S.; Calvino, J.; Cauqui, M.; Gatica, J.; Larese, C.; Pérez Omil, J.; Pintado, J. Some Recent Results on Metal/Support Interaction Effects in NM/CeO<sub>2</sub> (NM: Noble Metal) Catalysts. *Catal. Today* **1999**, *50* (2), 175–206.
- (6) Melchionna, M.; Fornasiero, P. The Role of Ceria-Based Nanostructured Materials in Energy Applications. *Mater. Today* **2014**, *17* (7), 349–357.
- (7) Beck, A.; Huang, X.; Artiglia, L.; Zabilskiy, M.; Wang, X.; Rzepka, P.; Palagin, D.; Willinger, M.-G.; van Bokhoven, J. A. The Dynamics of Overlayer Formation on Catalyst Nanoparticles and Strong Metal-Support Interaction. *Nat. Commun.* **2020**, *11* (1), 3220.
- (8) Lu, Y.; Thompson, C.; Kunwar, D.; Datye, A. K.; Karim, A. M. Origin of the High CO Oxidation Activity on CeO<sub>2</sub> Supported Pt Nanoparticles: Weaker Binding of CO or Facile Oxygen Transfer from the Support? *ChemCatChem*. **2020**, *12* (6), 1726–1733.
- (9) Zheng, T.; He, J.; Zhao, Y.; Xia, W.; He, J. Precious Metal-Support Interaction in Automotive Exhaust Catalysts. *J. Rare Earths* **2014**, *32* (2), 97–107.
- (10) Zhou, Y.; Jin, C.; Li, Y.; Shen, W. Dynamic Behavior of Metal Nanoparticles for Catalysis. *Nano Today* **2018**, *20*, 101–120.
- (11) Montini, T.; Melchionna, M.; Monai, M.; Fornasiero, P. Fundamentals and Catalytic Applications of CeO<sub>2</sub>-Based Materials. *Chem. Rev.* **2016**, *116* (10), 5987–6041.
- (12) Trovarelli, A.; Llorca, J. Ceria Catalysts at Nanoscale: How Do Crystal Shapes Shape Catalysis? *ACS Catal.* **2017**, *7* (7), 4716–4735.
- (13) Gao, Y.; Wang, W.; Chang, S.; Huang, W. Morphology Effect of CeO<sub>2</sub> Support in the Preparation, Metal-Support Interaction, and Catalytic Performance of Pt/CeO<sub>2</sub> Catalysts. *ChemCatChem*. **2013**, *5* (12), 3610–3620.
- (14) Kourtelesis, M.; Moraes, T. S.; Mattos, L. V.; Niakolas, D. K.; Noronha, F. B.; Verykios, X. The Effects of Support Morphology on the Performance of Pt/CeO<sub>2</sub> Catalysts for the Low Temperature Steam Reforming of Ethanol. *Appl. Catal. B Environ.* **2021**, *284*, 119757.
- (15) Yu, L.; Peng, R.; Chen, L.; Fu, M.; Wu, J.; Ye, D. Ag Supported on CeO<sub>2</sub> with Different Morphologies for the Catalytic Oxidation of HCHO. *Chem. Eng. J.* **2018**, *334*, 2480–2487.
- (16) Wang, Z.; Huang, Z.; Brosnahan, J. T.; Zhang, S.; Guo, Y.; Guo, Y.; Wang, L.; Wang, Y.; Zhan, W. Ru/CeO<sub>2</sub> Catalyst with Optimized CeO<sub>2</sub> Support Morphology and Surface Facets for Propane Combustion. *Environ. Sci. Technol.* **2019**, *53* (9), 5349–5358.
- (17) Konsolakis, M.; Lykaki, M. Facet-Dependent Reactivity of Ceria Nanoparticles Exemplified by CeO<sub>2</sub>-Based Transition Metal Catalysts: A Critical Review. *Catalysts* **2021**, *11* (4), 452.
- (18) Jiang, B.; Li, C.; Dag, Ö.; Abe, H.; Takei, T.; Imai, T.; Hossain, M. S. A.; Islam, M. T.; Wood, K.; Henzie, J.; Yamauchi, Y. Mesoporous Metallic Rhodium Nanoparticles. *Nat. Commun.* **2017**, *8* (1), 1–8.
- (19) Li, W.; Liu, J.; Zhao, D. Mesoporous Materials for Energy Conversion and Storage Devices. *Nat. Rev. Mater.* **2016**, *1* (6), 1–17.
- (20) Yang, X.; Cheng, X.; Ma, J.; Zou, Y.; Luo, W.; Deng, Y. Large-Pore Mesoporous CeO<sub>2</sub>-ZrO<sub>2</sub> Solid Solutions with In-Pore Confined Pt Nanoparticles for Enhanced CO Oxidation. *Small* **2019**, *15* (39), 1903058.
- (21) Zhou, A.; Wang, J.; Wang, H.; Li, H.; Wang, J.; Shen, M. Effect of Active Oxygen on the Performance of Pt/CeO<sub>2</sub> Catalysts for CO Oxidation. *J. Rare Earths* **2018**, *36* (3), 257–264.
- (22) Ferré, G.; Aouine, M.; Bosselet, F.; Burel, L.; Cadete Santos Aires, F. J.; Geantet, C.; Ntais, S.; Maurer, F.; Casapu, M.; Grunwaldt, J.-D.; Epicier, T.; Lorient, S.; Vernoux, P. Exploiting the Dynamic Properties of Pt on Ceria for Low-Temperature CO Oxidation. *Catal. Sci. Technol.* **2020**, *10* (12), 3904–3917.
- (23) Gänzler, A. M.; Casapu, M.; Doronkin, D. E.; Maurer, F.; Lott, P.; Glatzel, P.; Votsmeier, M.; Deutschmann, O.; Grunwaldt, J. Unravelling the Different Reaction Pathways for Low Temperature CO Oxidation on Pt/CeO<sub>2</sub> and Pt/Al<sub>2</sub>O<sub>3</sub> by Spatially Resolved Structure–Activity Correlations. *J. Phys. Chem. Lett.* **2019**, *10* (24), 7698–7705.
- (24) Gänzler, A. M.; Casapu, M.; Vernoux, P.; Lorient, S.; Cadete Santos Aires, F. J.; Epicier, T.; Betz, B.; Hoyer, R.; Grunwaldt, J.-D. Tuning the Structure of Pt Particles on Ceria in Situ for Enhancing the Catalytic Performance of Exhaust Gas Catalysts. *Angew. Chemie Int. Ed.* **2017**, *56*, 13078–13082.
- (25) Ogel, E.; Casapu, M.; Doronkin, D. E.; Popescu, R.; Störmer, H.; Mechler, C.; Marzun, G.; Barcikowski, S.; Türk, M.; Grunwaldt, J.-D. Impact of Preparation Method and Hydrothermal Aging on Particle Size Distribution of Pt/ $\gamma$ -Al<sub>2</sub>O<sub>3</sub> and Its Performance in CO and NO Oxidation. *J. Phys. Chem. C* **2019**, *123* (9), 5433–5446.
- (26) Casapu, M.; Fischer, A.; Gänzler, A. M.; Popescu, R.; Crone, M.; Gerthsen, D.; Türk, M.; Grunwaldt, J.-D. Origin of the Normal and Inverse Hysteresis Behavior during CO Oxidation over Pt/Al<sub>2</sub>O<sub>3</sub>. *ACS Catal.* **2017**, *7* (1), 343–355.
- (27) Farmer, J. A.; Campbell, C. T. Ceria Maintains Smaller Metal Catalyst Particles by Strong Metal-Support Bonding. *Science* **2010**, *329* (5994), 933–936.
- (28) Nagai, Y.; Hirabayashi, T.; Dohmae, K.; Takagi, N.; Minami, T.; Shinjoh, H.; Matsumoto, S. Sintering Inhibition Mechanism of

Platinum Supported on Ceria-Based Oxide and Pt-Oxide-Support Interaction. *J. Catal.* **2006**, *242* (1), 103–109.

(29) Bruix, A.; Rodriguez, J. A.; Ramirez, P. J.; Senanayake, S. D.; Evans, J.; Park, J. B.; Stacchiola, D.; Liu, P.; Hrbek, J.; Illas, F. A New Type of Strong Metal–Support Interaction and the Production of H<sub>2</sub> through the Transformation of Water on Pt/CeO<sub>2</sub> (111) and Pt/CeO<sub>x</sub>/TiO<sub>2</sub> (110) Catalysts. *J. Am. Chem. Soc.* **2012**, *134* (21), 8968–8974.

(30) Daelman, N.; Capdevila-Cortada, M.; López, N. Dynamic Charge and Oxidation State of Pt/CeO<sub>2</sub> Single-Atom Catalysts. *Nat. Mater.* **2019**, *18* (11), 1215–1221.

(31) Meunier, F. C.; Cardenas, L.; Kaper, H.; Šmíd, B.; Vorokhta, M.; Grosjean, R.; Aubert, D.; Dembélé, K.; Lunkenbein, T. Synergy between Metallic and Oxidized Pt Sites Unravelling during Room Temperature CO Oxidation on Pt/Ceria. *Angew. Chemie Int. Ed.* **2021**, *60* (7), 3799–3805.

(32) Maurer, F.; Gänzler, A.; Lott, P.; Betz, B.; Votsmeier, M.; Loidant, S.; Vernoux, P.; Murzin, V.; Bornmann, B.; Frahm, R.; Deutschmann, O.; Casapu, M.; Grunwaldt, J.-D. Spatiotemporal Investigation of the Temperature and Structure of a Pt/CeO<sub>2</sub> Oxidation Catalyst for CO and Hydrocarbon Oxidation during Pulse Activation. *Ind. Eng. Chem. Res.* **2021**, *60*, 6662–6675.

(33) Beck, A.; Zabilskiy, M.; Newton, M. A.; Safonova, O.; Willinger, M. G.; van Bokhoven, J. A. Following the Structure of Copper-Zinc-Alumina across the Pressure Gap in Carbon Dioxide Hydrogenation. *Nat. Catal.* **2021**, *4* (6), 488–497.

(34) Hatanaka, M.; Takahashi, N.; Takahashi, N.; Tanabe, T.; Nagai, Y.; Suda, A.; Shinjoh, H. Reversible Changes in the Pt Oxidation State and Nanostructure on a Ceria-Based Supported Pt. *J. Catal.* **2009**, *266* (2), 182–190.

(35) Nagai, Y.; Dohmae, K.; Ikeda, Y.; Takagi, N.; Hara, N.; Tanabe, T.; Guilera, G.; Pascarelli, S.; Newton, M. A.; Takahashi, N.; Shinjoh, H.; Matsumoto, S. In Situ Observation of Platinum Sintering on Ceria-Based Oxide for Autoexhaust Catalysts Using Turbo-XAS. *Catal. Today* **2011**, *175* (1), 133–140.

(36) Nagai, Y.; Dohmae, K.; Ikeda, Y.; Takagi, N.; Tanabe, T.; Hara, N.; Guilera, G.; Pascarelli, S.; Newton, M. A.; Kuno, O.; Jiang, H.; Shinjoh, H.; Matsumoto, S. In Situ Redispersion of Platinum Autoexhaust Catalysts: An On-Line Approach to Increasing Catalyst Lifetimes? *Angew. Chemie Int. Ed.* **2008**, *47* (48), 9303–9306.

(37) Li, Y.; Kottwitz, M.; Vincent, J. L.; Enright, M. J.; Liu, Z.; Zhang, L.; Huang, J.; Senanayake, S. D.; Yang, W. C. D.; Crozier, P. A.; Nuzzo, R. G.; Frenkel, A. I. Dynamic Structure of Active Sites in Ceria-Supported Pt Catalysts for the Water Gas Shift Reaction. *Nat. Commun.* **2021**, *12* (1), 1–9.

(38) Maurer, F.; Jelic, J.; Wang, J.; Gänzler, A.; Dolcet, P.; Wöll, C.; Wang, Y.; Studt, F.; Casapu, M.; Grunwaldt, J.-D. Tracking the Formation, Fate and Consequence for Catalytic Activity of Pt Single Sites on CeO<sub>2</sub>. *Nat. Catal.* **2020**, *3* (10), 824–833.

(39) Beck, A.; Frey, H.; Becker, M.; Artiglia, L.; Willinger, M. G.; van Bokhoven, J. A. Influence of Hydrogen Pressure on the Structure of Platinum–Titania Catalysts. *J. Phys. Chem. C* **2021**, *125*, 22531.

(40) Li, X.; Wang, X.; Sadykov, I. I.; Palagin, D.; Safonova, O. V.; Li, J.; Beck, A.; Krumeich, F.; van Bokhoven, J. A.; Artiglia, L. Temperature and Reaction Environment Influence the Nature of Platinum Species Supported on Ceria. *ACS Catal.* **2021**, *11* (21), 13041–13049.

(41) Jones, J.; Xiong, H.; DeLaRiva, A. T.; Peterson, E. J.; Pham, H.; Challa, S. R.; Qi, G.; Oh, S.; Wiebenga, M. H.; Pereira Hernandez, X. I.; Wang, Y.; Datye, A. K. Thermally Stable Single-Atom Platinum-on-Ceria Catalysts via Atom Trapping. *Science* **2016**, *353* (6295), 150–154.

(42) Pereira-Hernández, X. I.; DeLaRiva, A.; Muravev, V.; Kunwar, D.; Xiong, H.; Sudduth, B.; Engelhard, M.; Kovarik, L.; Hensen, E. J. M.; Wang, Y.; Datye, A. K. Tuning Pt-CeO<sub>2</sub> Interactions by High-Temperature Vapor-Phase Synthesis for Improved Reducibility of Lattice Oxygen. *Nat. Commun.* **2019**, *10* (1), 1358.

(43) Kunwar, D.; Zhou, S.; DeLaRiva, A.; Peterson, E. J.; Xiong, H.; Pereira-Hernández, X. I.; Purdy, S. C.; ter Veen, R.; Brongersma, H. H.; Miller, J. T.; Hashiguchi, H.; Kovarik, L.; Lin, S.; Guo, H.; Wang, Y.; Datye, A. K. Stabilizing High Metal Loadings of Thermally Stable

Platinum Single Atoms on an Industrial Catalyst Support. *ACS Catal.* **2019**, *9* (5), 3978–3990.

(44) Gänzler, A. M.; Casapu, M.; Maurer, F.; Störmer, H.; Gerthsen, D.; Ferré, G.; Vernoux, P.; Bornmann, B.; Frahm, R.; Murzin, V.; Nachttegaal, M.; Votsmeier, M.; Grunwaldt, J.-D. Tuning the Pt/CeO<sub>2</sub> Interface by in Situ Variation of the Pt Particle Size. *ACS Catal.* **2018**, *8* (6), 4800–4811.

(45) Resasco, J.; DeRita, L.; Dai, S.; Chada, J. P.; Xu, M.; Yan, X.; Finzel, J.; Hanukovich, S.; Hoffman, A. S.; Graham, G. W.; Bare, S. R.; Pan, X.; Christopher, P. Uniformity Is Key in Defining Structure–Function Relationships for Atomically Dispersed Metal Catalysts: The Case of Pt/CeO<sub>2</sub>. *J. Am. Chem. Soc.* **2020**, *142* (1), 169–184.

(46) Goodman, E. D.; Johnston-Peck, A. C.; Dietze, E. M.; Wrasman, C. J.; Hoffman, A. S.; Abild-Pedersen, F.; Bare, S. R.; Plessow, P. N.; Cargnello, M. Catalyst Deactivation via Decomposition into Single Atoms and the Role of Metal Loading. *Nat. Catal.* **2019**, *2* (9), 748–755.

(47) Nguyen, T. S.; Morfin, F.; Aouine, M.; Bosselet, F.; Rousset, J. L.; Piccolo, L. Trends in the CO Oxidation and PROX Performances of the Platinum-Group Metals Supported on Ceria. *Catal. Today* **2015**, *253*, 106–114.

(48) Chen, J.; Wanyan, Y.; Zeng, J.; Fang, H.; Li, Z.; Dong, Y.; Qin, R.; Wu, C.; Liu, D.; Wang, M.; Kuang, Q.; Xie, Z.; Zheng, L. Surface Engineering Protocol To Obtain an Atomically Dispersed Pt/CeO<sub>2</sub> Catalyst with High Activity and Stability for CO Oxidation. *ACS Sustain. Chem. Eng.* **2018**, *6* (11), 14054–14062.

(49) Bera, P.; Gayen, A.; Hegde, M. S.; Lalla, N. P.; Spadaro, L.; Frusteri, F.; Arena, F. Promoting Effect of CeO<sub>2</sub> in Combustion Synthesized Pt/CeO<sub>2</sub> Catalyst for CO Oxidation. *J. Phys. Chem. B* **2003**, *107* (25), 6122–6130.

(50) Liu, J. Scanning Transmission Electron Microscopy and Its Application to the Study of Nanoparticles and Nanoparticle Systems. *J. Electron Microsc. (Tokyo)*. **2005**, *54* (3), 251–278.

(51) Cargnello, M.; Doan-Nguyen, V. V. T.; Gordon, T. R.; Diaz, R. E.; Stach, E. a.; Gorte, R. J.; Fornasiero, P.; Murray, C. B. Control of Metal Nanocrystal Size Reveals Metal-Support Interface Role for Ceria Catalysts. *Science* **2013**, *341* (6147), 771–773.

(52) Bruix, A.; Neyman, K. M. Modeling Ceria-Based Nanomaterials for Catalysis and Related Applications. *Catal. Lett.* **2016**, *146* (10), 2053–2080.

(53) An, K.; Alayoglu, S.; Musselwhite, N.; Plamthottam, S.; Melaet, G.; Lindeman, A. E.; Somorjai, G. A. Enhanced CO Oxidation Rates at the Interface of Mesoporous Oxides and Pt Nanoparticles. *J. Am. Chem. Soc.* **2013**, *135* (44), 16689–16696.

(54) Boronin, A. I.; Slavinskaya, E. M.; Figueroba, A.; Stadnichenko, A. I.; Kardash, T. Y.; Stonkus, O. A.; Fedorova, E. A.; Muravev, V. V.; Svetlichnyi, V. A.; Bruix, A.; Neyman, K. M. CO Oxidation Activity of Pt/CeO<sub>2</sub> Catalysts below 0 °C: Platinum Loading Effects. *Appl. Catal. B Environ.* **2021**, *286*, 119931.

(55) Singhania, N.; Anumol, E. A.; Ravishankar, N.; Madras, G. Influence of CeO<sub>2</sub> Morphology on the Catalytic Activity of CeO<sub>2</sub>–Pt Hybrids for CO Oxidation. *Dalt. Trans.* **2013**, *42* (43), 15343.

(56) Chen, M.; Zheng, Y.; Wan, H. Kinetics and Active Surfaces for CO Oxidation on Pt-Group Metals under Oxygen Rich Conditions. *Top. Catal.* **2013**, *56* (15–17), 1299–1313.

(57) Kopelent, R.; van Bokhoven, J. A.; Szlachetko, J.; Edebeli, J.; Paun, C.; Nachttegaal, M.; Safonova, O. V. Catalytically Active and Spectator Ce<sup>3+</sup> in Ceria-Supported Metal Catalysts. *Angew. Chemie Int. Ed.* **2015**, *54* (30), 8728–8731.

(58) Morfin, F.; Nguyen, T. S.; Rousset, J. L.; Piccolo, L. Synergy between Hydrogen and Ceria in Pt-Catalyzed CO Oxidation: An Investigation on Pt–CeO<sub>2</sub> Catalysts Synthesized by Solution Combustion. *Appl. Catal. B Environ.* **2016**, *197*, 2–13.

(59) Ke, J.; Zhu, W.; Jiang, Y.; Si, R.; Wang, Y.-J.; Li, S.-C.; Jin, C.; Liu, H.; Song, W.-G.; Yan, C.-H.; Zhang, Y.-W. Strong Local Coordination Structure Effects on Subnanometer PtO<sub>x</sub> Clusters over CeO<sub>2</sub> Nanowires Probed by Low-Temperature CO Oxidation. *ACS Catal.* **2015**, *5* (9), 5164–5173.

- (60) Shimada, S.; Takei, T.; Akita, T.; Takeda, S.; Haruta, M. Influence of the Preparation Methods for Pt/CeO<sub>2</sub> and Au/CeO<sub>2</sub> Catalysts in CO Oxidation. *Stud. Surf. Sci. Catal.* **2010**, *175* (2), 843–847.
- (61) Lee, J.; Ryou, Y.; Kim, J.; Chan, X.; Kim, T. J.; Kim, D. H. Influence of the Defect Concentration of Ceria on the Pt Dispersion and the CO Oxidation Activity of Pt/CeO<sub>2</sub>. *J. Phys. Chem. C* **2018**, *122* (9), 4972–4983.
- (62) Mai, H.-X.; Sun, L.-D.; Zhang, Y.-W.; Si, R.; Feng, W.; Zhang, H.-P.; Liu, H.-C.; Yan, C.-H. Shape-Selective Synthesis and Oxygen Storage Behavior of Ceria Nanopolyhedra, Nanorods, and Nanocubes. *J. Phys. Chem. B* **2005**, *109* (51), 24380–24385.
- (63) Schindelin, J.; Arganda-Carreras, I.; Frise, E.; Kaynig, V.; Longair, M.; Pietzsch, T.; Preibisch, S.; Rueden, C.; Saalfeld, S.; Schmid, B.; Tinevez, J. Y.; White, D. J.; Hartenstein, V.; Eliceiri, K.; Tomancak, P.; Cardona, A. Fiji: An Open-Source Platform for Biological-Image Analysis. *Nat. Methods* **2012**, *9* (7), 676–682.
- (64) Brunauer, S.; Emmett, P. H.; Teller, E. Adsorption of Gases in Multimolecular Layers. *J. Am. Chem. Soc.* **1938**, *60* (2), 309–319.
- (65) Zimina, A.; Dardenne, K.; Denecke, M. A.; Doronkin, D. E.; Huttel, E.; Lichtenberg, H.; Mangold, S.; Pruessmann, T.; Rothe, J.; Spangenberg, T.; Steininger, R.; Vitova, T.; Geckeis, H.; Grunwaldt, J.-D. CAT-ACT—A New Highly Versatile X-Ray Spectroscopy Beamline for Catalysis and Radionuclide Science at the KIT Synchrotron Light Facility ANKA. *Rev. Sci. Instrum.* **2017**, *88* (11), 113113.
- (66) Grunwaldt, J.-D.; Caravati, M.; Hannemann, S.; Baiker, A. X-Ray Absorption Spectroscopy under Reaction Conditions: Suitability of Different Reaction Cells for Combined Catalyst Characterization and Time-Resolved Studies. *Phys. Chem. Chem. Phys.* **2004**, *6* (11), 3037–3047.
- (67) Welter, E.; Chernikov, R.; Herrmann, M.; Nemausat, R. A Beamline for Bulk Sample X-Ray Absorption Spectroscopy at the High Brilliance Storage Ring PETRA III. *AIP Conf. Proc.* **2018**, *2054* (1), 040002.
- (68) Meunier, F. C. The Design and Testing of Kinetically-Appropriate Operando Spectroscopic Cells for Investigating Heterogeneous Catalytic Reactions. *Chem. Soc. Rev.* **2010**, *39* (12), 4602.
- (69) Agostini, G.; Meira, D.; Monte, M.; Vitoux, H.; Iglesias-Juez, A.; Fernández-García, M.; Mathon, O.; Meunier, F.; Berruyer, G.; Perrin, F.; Pasternak, S.; Mairs, T.; Pascarelli, S.; Gorges, B. XAS/DRIFTS/MS Spectroscopy for Time-Resolved Operando Investigations at High Temperature. *J. Synchrotron Radiat.* **2018**, *25* (6), 1745–1752.
- (70) Kresse, G.; Furthmüller, J. Efficient Iterative Schemes for *Ab Initio* Total-Energy Calculations Using a Plane-Wave Basis Set. *Phys. Rev. B* **1996**, *54* (16), 11169–11186.
- (71) Kresse, G.; Furthmüller, J. Efficiency of *Ab-Initio* Total Energy Calculations for Metals and Semiconductors Using a Plane-Wave Basis Set. *Comput. Mater. Sci.* **1996**, *6* (1), 15–50.
- (72) Bahn, S. R.; Jacobsen, K. W. An Object-Oriented Scripting Interface to a Legacy Electronic Structure Code. *Comput. Sci. Eng.* **2002**, *4* (3), 56–66.
- (73) Blöchl, P. E. Projector Augmented-Wave Method. *Phys. Rev. B* **1994**, *50* (24), 17953–17979.
- (74) Kresse, G.; Joubert, D. From Ultrasoft Pseudopotentials to the Projector Augmented-Wave Method. *Phys. Rev. B* **1999**, *59* (3), 1758–1775.
- (75) Wellendorff, J.; Lundgaard, K. T.; Mogelhøj, A.; Petzold, V.; Landis, D. D.; Nørskov, J. K.; Bligaard, T.; Jacobsen, K. W. Density Functionals for Surface Science: Exchange-Correlation Model Development with Bayesian Error Estimation. *Phys. Rev. B* **2012**, *85* (23), 235149.
- (76) Dudarev, S. L.; Botton, G. A.; Savrasov, S. Y.; Humphreys, C. J.; Sutton, A. P. Electron-Energy-Loss Spectra and the Structural Stability of Nickel Oxide: An LSDA+U Study. *Phys. Rev. B* **1998**, *57* (3), 1505–1509.
- (77) Monkhorst, H. J.; Pack, J. D. Special Points for Brillouin-Zone Integrations. *Phys. Rev. B* **1976**, *13* (12), 5188–5192.
- (78) Lee, J.; Ryou, Y.; Chan, X.; Kim, T. J.; Kim, D. H. How Pt Interacts with CeO<sub>2</sub> under the Reducing and Oxidizing Environments at Elevated Temperature: The Origin of Improved Thermal Stability of Pt/CeO<sub>2</sub> Compared to CeO<sub>2</sub>. *J. Phys. Chem. C* **2016**, *120* (45), 25870–25879.
- (79) Gänzler, A. M.; Casapu, M.; Doronkin, D. E.; Maurer, F.; Lott, P.; Glatzel, P.; Votsmeier, M.; Deutschmann, O.; Grunwaldt, J.-D. Unravelling the Different Reaction Pathways for Low Temperature CO Oxidation on Pt/CeO<sub>2</sub> and Pt/Al<sub>2</sub>O<sub>3</sub> by Spatially Resolved Structure-Activity Correlations. *J. Phys. Chem. Lett.* **2019**, *10* (24), 7698–7705.
- (80) Liu, H. H.; Wang, Y.; Jia, A. P.; Wang, S. Y.; Luo, M. F.; Lu, J. Q. Oxygen Vacancy Promoted CO Oxidation over Pt/CeO<sub>2</sub> Catalysts: A Reaction at Pt-CeO<sub>2</sub> Interface. *Appl. Surf. Sci.* **2014**, *314*, 725–734.
- (81) Daniel, M.; Loridant, S. Probing Reoxidation Sites by in Situ Raman Spectroscopy: Differences between Reduced CeO<sub>2</sub> and Pt/CeO<sub>2</sub>. *J. Raman Spectrosc.* **2012**, *43* (9), 1312–1319.
- (82) Agarwal, S.; Zhu, X.; Hensen, E. J. M.; Mojet, B. L.; Lefferts, L. Surface-Dependence of Defect Chemistry of Nanostructured Ceria. *J. Phys. Chem. C* **2015**, *119* (22), 12423–12433.
- (83) Weber, W. H.; Hass, K. C.; McBride, J. R. Raman Study of CeO<sub>2</sub>: Second-Order Scattering, Lattice Dynamics, and Particle-Size Effects. *Phys. Rev. B* **1993**, *48* (1), 178–185.
- (84) Wu, Z.; Li, M.; Howe, J.; Meyer, H. M.; Overbury, S. H. Probing Defect Sites on CeO<sub>2</sub> Nanocrystals with Well-Defined Surface Planes by Raman Spectroscopy and O<sub>2</sub> Adsorption. *Langmuir* **2010**, *26* (21), 16595–16606.
- (85) Lin, W.; Herzog, A. A.; Kiely, C. J.; Wachs, I. E. Probing Metal-Support Interactions under Oxidizing and Reducing Conditions: In Situ Raman and Infrared Spectroscopic and Scanning Transmission Electron Microscopic-X-Ray Energy-Dispersive Spectroscopic Investigation of Supported Platinum Catalysts. *J. Phys. Chem. C* **2008**, *112* (15), 5942–5951.
- (86) Brogan, M. S.; Dines, T. J.; Cairns, J. A. Raman Spectroscopic Study of the Pt–CeO<sub>2</sub> Interaction in the Pt/Al<sub>2</sub>O<sub>3</sub>–CeO<sub>2</sub> Catalyst. *J. Chem. Soc., Faraday Trans.* **1994**, *90* (10), 1461–1466.
- (87) Kale, M. J.; Christopher, P. Utilizing Quantitative in Situ FTIR Spectroscopy To Identify Well-Coordinated Pt Atoms as the Active Site for CO Oxidation on Al<sub>2</sub>O<sub>3</sub>-Supported Pt Catalysts. *ACS Catal.* **2016**, *6* (8), 5599–5609.
- (88) Green, I. X.; Tang, W.; Neurock, M.; Yates, J. T. Spectroscopic Observation of Dual Catalytic Sites During Oxidation of CO on a Au/TiO<sub>2</sub> Catalyst. *Science* **2011**, *333* (6043), 736–739.
- (89) Avanesian, T.; Dai, S.; Kale, M. J.; Graham, G. W.; Pan, X.; Christopher, P. Quantitative and Atomic-Scale View of CO-Induced Pt Nanoparticle Surface Reconstruction at Saturation Coverage via DFT Calculations Coupled with in Situ TEM and IR. *J. Am. Chem. Soc.* **2017**, *139* (12), 4551–4558.
- (90) Bazin, P.; Saur, O.; Lavalley, J. C.; Daturi, M.; Blanchard, G. FT-IR Study of CO Adsorption on Pt/CeO<sub>2</sub>: Characterisation and Structural Rearrangement of Small Pt Particles. *Phys. Chem. Chem. Phys.* **2005**, *7* (1), 187–194.
- (91) Barrabés, N.; Föttinger, K.; Dafinov, A.; Medina, F.; Rupprechter, G.; Llorca, J.; Sueiras, J. E. Study of Pt-CeO<sub>2</sub> Interaction and the Effect in the Selective Hydrodechlorination of Trichloroethylene. *Appl. Catal. B Environ.* **2009**, *87* (1–2), 84–91.
- (92) Nie, L.; Mei, D.; Xiong, H.; Peng, B.; Ren, Z.; Hernandez, X. I. P.; DeLaRiva, A.; Wang, M.; Engelhard, M. H.; Kovarik, L.; Datye, A. K.; Wang, Y. Activation of Surface Lattice Oxygen in Single-Atom Pt/CeO<sub>2</sub> for Low-Temperature CO Oxidation. *Science* **2017**, *358* (6369), 1419–1423.
- (93) Meunier, F. C. Relevance of IR Spectroscopy of Adsorbed CO for the Characterization of Heterogeneous Catalysts Containing Isolated Atoms. *J. Phys. Chem. C* **2021**, *125* (40), 21810–21823.
- (94) Newton, M. A.; Ferri, D.; Smolentsev, G.; Marchionni, V.; Nachttegaal, M. Room-Temperature Carbon Monoxide Oxidation by Oxygen over Pt/Al<sub>2</sub>O<sub>3</sub> Mediated by Reactive Platinum Carbonates. *Nat. Commun.* **2015**, *6*, 8675.
- (95) Pilger, F.; Testino, A.; Carino, A.; Proff, C.; Kambolis, A.; Cervellino, A.; Ludwig, C. Size Control of Pt Clusters on CeO<sub>2</sub>

Nanoparticles via an Incorporation–Segregation Mechanism and Study of Segregation Kinetics. *ACS Catal.* **2016**, *6* (6), 3688–3699.

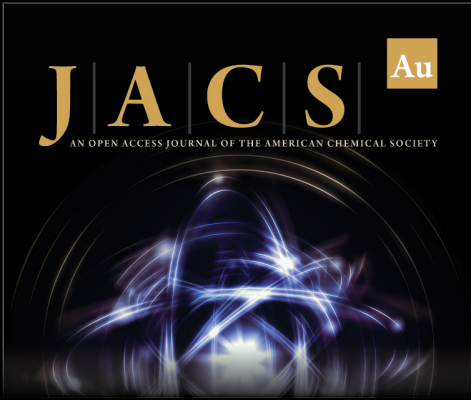
(96) Burada, P. S.; Hänggi, P.; Marchesoni, F.; Schmid, G.; Talkner, P. Diffusion in Confined Geometries. *ChemPhysChem* **2009**, *10* (1), 45–54.

(97) Liu, L.; Corma, A. Identification of the Active Sites in Supported Subnanometric Metal Catalysts. *Nat. Catal.* **2021**, *4* (6), 453–456.


(98) DeRita, L.; Dai, S.; Lopez-Zepeda, K.; Pham, N.; Graham, G. W.; Pan, X.; Christopher, P. Catalyst Architecture for Stable Single Atom Dispersion Enables Site-Specific Spectroscopic and Reactivity Measurements of CO Adsorbed to Pt Atoms, Oxidized Pt Clusters, and Metallic Pt Clusters on TiO<sub>2</sub>. *J. Am. Chem. Soc.* **2017**, *139* (40), 14150–14165.


(99) Wang, H.; Liu, J.-X.; Allard, L. F.; Lee, S.; Liu, J.; Li, H.; Wang, J.; Wang, J.; Oh, S. H.; Li, W.; Flytzani-Stephanopoulos, M.; Shen, M.; Goldsmith, B. R.; Yang, M. Surpassing the Single-Atom Catalytic Activity Limit through Paired Pt-O-Pt Ensemble Built from Isolated Pt<sub>1</sub> Atoms. *Nat. Commun.* **2019**, *10* (1), 3808.


(100) Hatanaka, M.; Takahashi, N.; Tanabe, T.; Nagai, Y.; Dohmae, K.; Aoki, Y.; Yoshida, T.; Shinjoh, H. Ideal Pt Loading for a Pt/CeO<sub>2</sub>-Based Catalyst Stabilized by a Pt-O-Ce Bond. *Appl. Catal. B Environ.* **2010**, *99* (1–2), 336–342.



**JACS** Au  
AN OPEN ACCESS JOURNAL OF THE AMERICAN CHEMICAL SOCIETY

 Editor-in-Chief  
**Prof. Christopher W. Jones**  
Georgia Institute of Technology, USA

**Open for Submissions** 

pubs.acs.org/jacsau  ACS Publications  
Most Trusted. Most Cited. Most Read.